ACS NANO

www.acsnano.org

ARTICLE

Reactive Oxygen Species-Responsive Polymer Drug Delivery System Targeted Oxidative Stressed Colon Cells to Ameliorate Colitis

Wo-Qi Cai,[#] Wanqi Liang,[#] Dong Li,[#] Wenli Dai, Zhishu Li, Xinlin Wei, Lizeng Cheng, Bo-Bo Zhang,* and Qiongqiong Yang*

Cite This: https://doi.org/10.1021/acsnano.4c14373

Read Online

ACCESS | Metrics & More | Article Recommendations | Supporting Information

ABSTRACT: **Ulcerative colitis (UC) is a chronic inflammatory condition that imposes a huge healthcare burden globally. The inflamed colon is marked by an abundance of positively charged proteins, increased reactive oxygen species (ROS), a disrupted intestinal barrier, and an imbalanced gut microbiome. Leveraging these features, we designed a negatively charged ROS-responsive nanocarrier using diselenide-bond-modified carboxymethyl cellulose (CMC) for the targeted delivery of curcumin, a natural ROS-scavenging antioxidant, to treat UC. The design rationale encompasses three key aspects: (1) the biocompatible and biodegradable CMC matrix stabilizes curcumin during digestion; (2) the diselenide bonds enable redox-triggered curcumin release at inflammatory sites, ensuring precise therapeutic action; and (3) the negative charge of the nanoparticles enhances interactions with positively charged proteins in inflamed colon tissues, improving site-specific accumulation. Experimental validation confirmed these design principles, demonstrating that the resulting nanoparticles effectively preserve curcumin during digestion and enable the ROS-responsive release of curcumin at inflamed sites. Additionally, these nanoparticles interact effectively with folic acid receptors (positively charged proteins) that are overexpressed on oxidatively stressed cell membranes, leading to specific accumulation in colitis tissue. Subsequently, the nanoparticles scavenge excessive ROS, restore intestinal barrier function, and modulate the gut microbiota. These synergistic actions collectively contribute to significant mitigation of colitis symptoms in both preventive and therapeutic regimens, suggesting a promising alternative therapeutic approach for UC.**

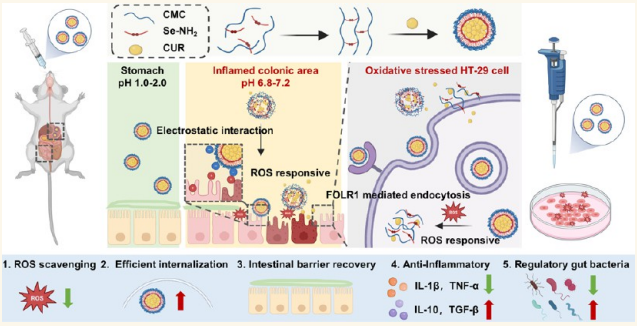

KEYWORDS: *reactive oxygen species, ROS-responsive, nanocarrier, oxidative stress, curcumin*

INTRODUCTION

Ulcerative colitis (UC) is a chronic inflammatory disorder of the colon primarily driven by an overactive immune response, resulting in inflammation of the intestinal lining and the underlying tissue.[1] There has been a significant increase in the prevalence of UC globally, especially in rapidly industrializing countries.[2,3] Many researchers consider that the invasion of toxins or harmful bacteria activates immune cells, leading to the production of numerous inflammatory cytokines and reactive oxygen species (ROS), resulting in the apoptosis of epithelial cells and reduced expression of tight junction proteins. This disruption compromises the gut lining, triggering inflammation that promotes UC development.[4] Despite advancements in conventional drug therapies, such as 5-aminosalicylic acid (5-ASA), many patients continue to experience inadequate symptom control and adverse effects.[5,6] The application of these drugs suffers from insufficient concentrations at the lesion site and lacks targeted distribution, making it difficult to achieve optimal therapeutic effects and resulting in organ toxicity.[7]

The development of intelligent drug carriers that allow for controlled drug release is essential for better colitis treatment. Numerous studies have demonstrated that individuals with UC have elevated levels of ROS in their intestinal mucosa.[8] From the perspective of drug delivery, the excessive ROS present in

Received: October 11, 2024
Revised: April 22, 2025
Accepted: April 23, 2025

inflamed colon tissue could serve as a precise biological cue for triggering an on-demand drug release within diseased microenvironments. This mechanism presents a promising avenue for developing smart, site-specific drug delivery platforms that respond to pathological conditions.[9] Based on the ROS-rich microenvironment, materials responsive to ROS stimuli, which can undergo bond cleavage (such as boronic ester,[10] proline,[11] and thioketal[12]) and solubility transformation (like thioether,[2] selenium,[13] or tellurium[14]), have been crafted for specific delivery to colon inflammation sites. Selenium-based polymers stand out as smart ROS-responsive biomaterials within the spectrum of ROS-sensitive compounds. These innovative materials undergo a remarkable transformation, shifting from water-repellent to water-soluble when exposed to high ROS concentrations. Researchers have successfully harnessed this unique property to engineer self-assembling nanoparticles for advanced applications.[15,16] The diselenide bond (Se−Se) is susceptible to oxidation, forming seleninic acid, or reduction, yielding selenodin, under different redox conditions.[17,18] In an intriguing process, selenodin under physiological conditions consumes $O_2^{\bullet}$ and is subsequently transformed back to a diselenide bond *via* dehydration.[19,20] In addition, diselenide bonds are recognized for their antioxidant properties and play a key role in maintaining the cellular redox balance. Therefore, diselenide bonds might work synergistically with model drugs to treat colitis, making diselenide-bond-containing polymers important and practical biomaterials for nanocarrier development. Based on the aforementioned reasons, we proposed that developing ROS-responsive nanocarriers with diselenide-bond-containing polymers for payload release in inflamed colons holds significant promise for the treatment of UC.

Carboxymethyl cellulose (CMC), a cellulose derivative approved by the US food and drug administration, is permitted to be used in clinical treatments.[21] CMC, as a polyanionic polymer, exhibits bioadhesive properties and pH sensitivity, making it an attractive platform for transdermal and transmucosal drug delivery in the treatment of UC.[22] Furthermore, due to the abundance of cationic proteins expressed in inflamed colon mucosa,[23] the anion nature of CMC allows it to adhere more easily to the affected area. Additionally, CMC can swell readily in the inflamed colon (pH 6.8−7.4), enhancing its effectiveness as a carrier for colon-targeted delivery.[22] These properties can also be further improved via chemical modifications. Given these characteristics, CMC is an ideal carrier for payload delivery, and increasing evidence suggests that a CMC polymer-based nanodrug delivery system can effectively treat UC, potentially serving as an alternative approach in the nanotherapeutics of UC.[24,25]

Curcumin (CUR) is a lipid-soluble bioactive substance, mainly isolated from the root of *Curcuma longa* L.[26] CUR has gained significant scientific attention due to its remarkable bioactive properties, such as antioxidant, anti-inflammatory, and anticancer, and ability to effectively treat and prevent human diseases.[27] Research has demonstrated that CUR exerts UC treatment effects by regulating key inflammatory mediators such as IL-1β, IFN-γ, TNF-α, and IL-6,[28] as well as their associated signaling pathways like MAPK/NF-κB/STAT3.[1] Recent advancements in gut microbiota research have also revealed that CUR can influence the composition of intestinal microbiota, increasing beneficial bacteria, enhancing the production of short-chain fatty acids (SCFAs), fortifying intestinal barrier integrity, and reducing the abundance of disease-associated pathogens like *Coriobacterales* and *Enterobacteria*.[29,30] These multifaceted effects synergistically contribute to alleviating symptoms and pathological progression in colitis. A major hurdle in employing CUR as an effective treatment is its unstable chemical nature and inadequate bioavailability, producing minimal or undetectable levels in blood and tissues beyond the intestines, along with swift metabolism and clearance from the body.[31−33] Thus, the development of effective delivery systems is urgently needed for harnessing CURs full therapeutic potential against specific colitis diseases.[34]

This study developed a novel ROS-responsive nanocarrier system using selenium-linked carboxymethyl cellulose (CMC-Se) for targeted CUR delivery to inflamed colon tissue (CUR@CMC-Se). The smart nanocarrier demonstrated dual functionality by both responding to and neutralizing ROS, effectively shielding HT29 cells and mouse colons from oxidative stress *in vitro* and *in vivo*. Leveraging the overexpression of folate receptors on oxidatively stressed colon cells, CUR@CMC-Se showed enhanced cellular uptake in inflamed HT29 and selective accumulation in colitis-affected colon regions following oral administration. CUR@CMC-Se ameliorated UC efficiently by targeted accumulation at colitis tissue, scavenging excessive ROS, regulating the expression of inflammatory cytokines, repairing mucosal barrier function, and regulating the homeostasis of gut microbiota. This nanocarrier shows minimal systemic toxicity and offers an alternative therapeutic approach to UC, addressing the limitations associated with CUR.

RESULTS

Synthesis and Characterization of CMC-Se. The synthetic routes of ROS-responsive block polymers Se-NHBoc, Se−NH_2, and CMC-Se are depicted in Figure S1. The synthesis process was validated through ^{1}H NMR spectroscopy, infrared (IR) spectroscopy, particle size analysis, transmission electron microscopy (TEM), X-ray photoelectron spectroscopy (XPS), and inductively coupled plasma-optical emission spectroscopy (ICP-OES). The ^{1}H NMR spectrum (Figure S2a) revealed characteristic proton signals for Se-NHBoc, with resonances appearing between 3.71 and 3.51 ppm (c, $-CH_2-$NHBoc, -Se-CH_2-CH_2-NH−) and 3.23 and 2.80 ppm (c, -Se-CH_2-CH_2-NH−). These findings confirm the successful conjugation of Fmoc-*D*-lys (Boc)−OH to 2−2′-diselanediyldiethanamine. After treatment with trifluoroacetic acid (TFA) in DCM (V/V = 1:4) at 25 °C overnight, the mixture was concentrated, yielding Se−NH_2. The ^{1}H NMR spectrum of Se−NH_2 (Figure S2b) displays a series of resonances, including 8.18 to 7.23 ppm (Fmoc), 4.51 to 4.19 ppm (a, Fmoc-linked −CH−CH_2-), 3.76 to 3.52 ppm (c, −CH_2-NH_2, -Se-CH_2-CH_2-NH−), 3.30 to 2.77 ppm (c, -Se-CH_2-CH_2-NH−), and 1.97 to 1.60 ppm (d, $-CH_2-CH_2-CH_2-$).

Subsequent condensation of CMC with Se−NH_2 resulted in the formation of CMC-Se. The integration of CMC-Se is confirmed by the distinct peaks observed from both CMC and Se−NH_2 in the ^{1}H NMR spectrum of CMC-Se (Figure S3). The IR spectrum of CMC-Se further confirmed the successful conjugation of Se−NH_2, displaying distinct absorption bands at 1690.88 cm^{-1} (−CO−NH−)[35] and 552.95 cm^{-1} (−Se−Se-), along with characteristic C−Se vibrations at 1233.92 cm^{-1} and 951.83 cm^{-1} (Figure S4a).[36] TEM imaging revealed CMC-Se's spherical morphology, while ICP-OES analysis demonstrated selenium's predominant surface distribution,

https://doi.org/10.1021/acsnano.4c14373
ACS Nano XXXX, XXX, XXX−XXX

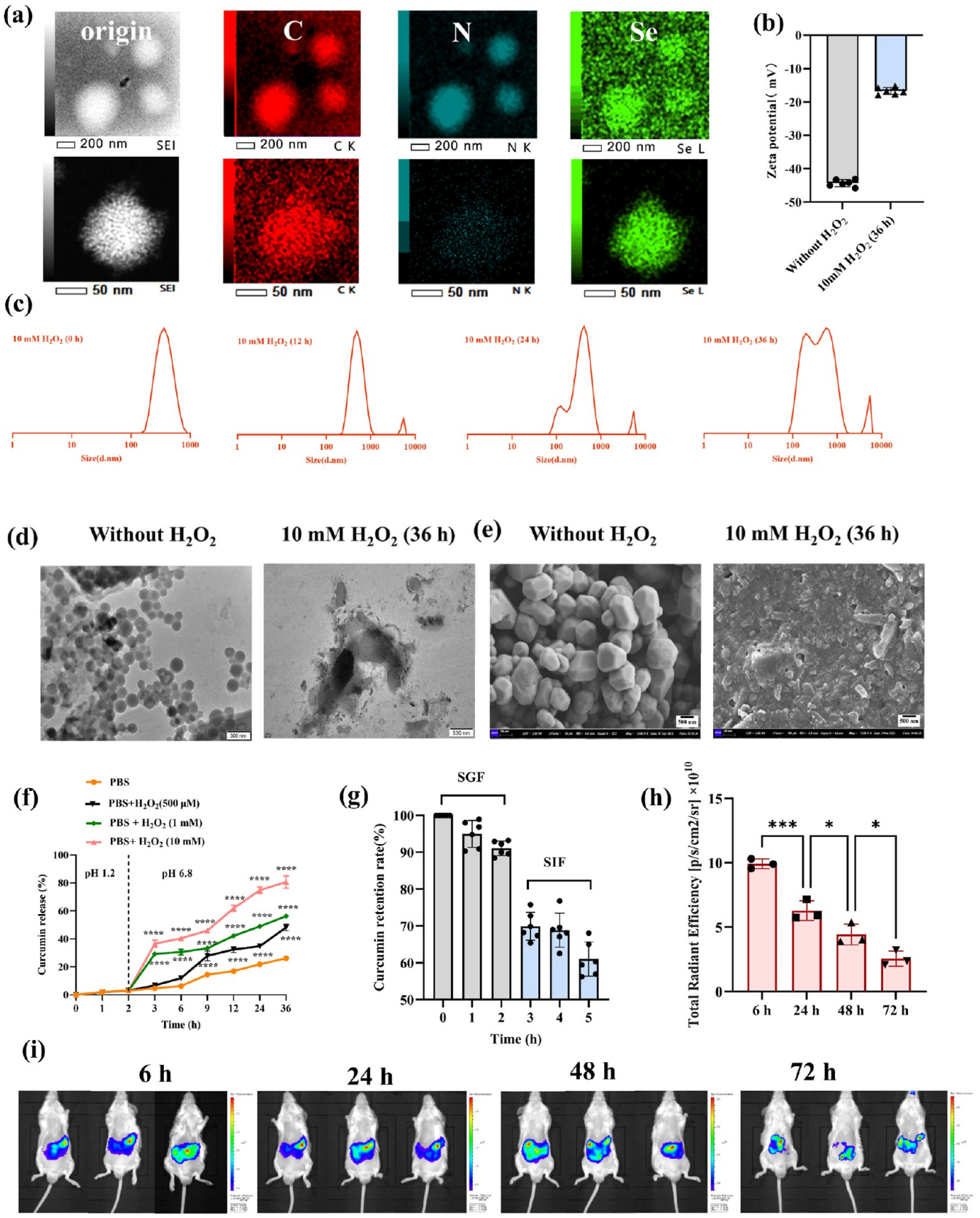

Figure 1. Characterization of CMC-Se and CUR@CMC-Se. (a) EDX of CMC-Se, (b) zeta potential of CUR@CMC-Se with and without H_2O_2, (c) particle distribution of CUR@CMC-Se with and without H_2O_2, (d) TEM images pf CUR@CMC-Se with and without H_2O_2, (e) SEM images of CUR@CMC-Se with and without H_2O_2, (f) curcumin release from CUR@CMC-Se in response to different concentrations of H_2O_2, (g) curcumin retention rate during simulated gastric-intestinal digestions, (h) fluorescence quantitative analysis of CUR@CMC-Se in UC mice at varied time intervals, and (i) corresponding fluorescence imaging of CUR@CMC-Se inside living mice at various time points.

https://doi.org/10.1021/acsnano.4c14373
ACS Nano XXXX, XXX, XXX−XXX

constituting 4.68% of the total elemental composition (Figures 1a and S4e,f). These findings collectively verify the structural integrity and elemental distribution of the synthesized material.

The ROS-responsive behavior of CMC-Se was assessed through incubation with 10 mM H_2O_2 for 36 h. As illustrated in Figure S4a, the distinctive Se−Se bond peak at 552.95 cm^{-1} vanished, confirming the bond cleavage upon H_2O_2 exposure. Subsequent selenium binding energy analysis revealed an oxidation state transition, with spin−orbit coupling data showing a prominent peak shift from 55.9 eV ($3d^5$) to 59.5 eV (Figure S4b), suggesting selenium oxidation to higher energy states forming selenite or oxidized species.[37] Dynamic light scattering (DLS) and TEM analyses showed marked structural changes, with CMC-Se's initially uniform spherical morphology transforming into disorganized aggregates, a significantly broadened particle size distribution (from 310.7 nm to 420−4702 nm) after oxidation, and a reduced stability indicated by the zeta potential shift from −35.67 to −22.32 mV (Figure S4c−e).[32] These findings collectively demonstrate that CMC-Se is suitable as an ROS-responsive nanocarrier capable of targeted drug release in inflamed colonic environments.

Preparation and Characterization of CUR@CMC-Se. To enable inflamed colon-specific and on-demand release of CUR, we developed a soluble ROS-responsive drug delivery system composed of a CMC-Se polymer nanocarrier to encapsulate CUR in the hydrophobic core. The graphical abstract illustrates the schematic diagram and the appearance of the nanoparticles. CUR@CMC-Se was prepared *via* a precipitation−ultrasonication method.[32] Untreated CMC showed a low CUR loading capacity of only 0.16%. In contrast, CMC-Se significantly increased this capacity to 4.87%, marking a 30.43-fold enhancement. DLS analysis showed that the zeta potential, particle size, and polydispersity index (PDI) of CUR@CMC-Se are −44.35 mV, 387.12 nm, and 0.212, respectively (Figure 1b,c), indicating a uniform dispersion in aqueous solution. To further confirm the successful preparation of CUR@CMC-Se, the samples were analyzed with FTIR and Different Scanning Calorimetry (DSC). As shown in Figure S5a, free CUR exhibited characteristic peaks at 3503.83 cm^{-1} (OH stretching), 1626.47 cm^{-1} (inter-ring C═C and C═O vibrations), and 1605.84 cm^{-1} (aromatic ring C═C stretching). In the spectrum of CUR@CMC-Se, these peaks disappeared, and the C−Se signal at 951.8 cm^{-1} weakened, possibly due to $\pi-\pi$ stacking interactions between CURs aromatic rings and Fmoc groups on CMC-Se, resulting in a diminished C−Se signal.[38] The DSC results showed that the characteristic endothermic peak of CUR at 185 °C vanished in CUR@CMC-Se (Figure S5b),[39] suggesting a transition from a crystalline to an amorphous state, possibly caused by strong $\pi-\pi$ stacking interactions between Fmoc groups in CMC-Se and CUR's aromatic ring-like molecules. All of these results demonstrated that CUR was successfully loaded within the CMC-Se nanocarrier.

ROS-Responsive Hydrolysis and CUR Release Profiles of CUR@CMC-Se. To evaluate the ROS-responsive capability of CUR@CMC-Se, H_2O_2, a member of ROS, was used to simulate the ROS environment. As shown in Figure 1b, after the incubation of CUR@CMC-Se with 10 mM H_2O_2 for 36 h, the zeta potential changed from −44.35 to −16.67 mV, which is an unstable state, indicating that the stable CUR@CMC-Se system was destroyed. In addition, the DLS results indicated a time-dependent increase in the size of CUR@CMC-Se in distilled water containing 10 mM H_2O_2 (Figure 1c). The change in the size and morphology of CUR@CMC-Se under 0 and 10 mM H_2O_2 determined using TEM and SEM are consistent with the DLS results. It is evident that following ROS-responsive hydrolysis, CUR was released from the nanocarriers (Figure 1d,e). Therefore, we further evaluated the ROS-responsive CUR release profile of CUR@CMC-Se. The oxidative-stress-triggered release efficiency of CUR@CMC-Se *in vitro* was examined by incubating CUR@CMC-Se in PBS (pH 1.2) for 2 h, after which the incubation conditions were changed to PBS (pH 6.8) containing different concentrations of H_2O_2. As shown in Figure 1f, the results revealed a gradual release pattern (around 5%) in PBS (pH 1.2) without H_2O_2 over 2 h, which suggested that CUR@CMC-Se can resist gastric digestion, effectively reducing the premature release of CUR. Upon entering the intestinal environment containing H_2O_2, a significant burst release phenomenon was observed. Notably, the CUR release rate correlated positively with H_2O_2 concentration, illustrating its skill in fine-tuning drug delivery in sync with the extent of inflammation. This capability effectively curbs unspecific drug release and minimizes the chance of adverse effects.

Stability Analysis of CUR@CMC-Se. Due to CUR's susceptibility to metabolism and enzymatic degradation during digestion, its oral bioavailability is typically low, making it challenging to achieve therapeutic levels even at high doses.[40] Therefore, enhancing CUR's bioavailability is crucial for improving its therapeutic efficacy. We examined the stability of CUR under simulated pH conditions, mimicking different parts of the digestive tract. Our findings demonstrate that CMC-Se effectively protects CUR from degradation caused by pH variations (Figure S6), indicating its stability during digestion. Furthermore, we evaluated the digestion resistance of CUR@CMC-Se using artificial simulated digestive fluids containing gastric mucin, ions, and the corresponding digestive enzymes. As shown in Figure 1g, after 2 h of gastric digestion, only 10% of CUR was lost, indicating that CMC-Se can efficiently resist the digestion of gastric fluids. Thereafter, after 3 h of simulated intestinal digestion, more than 60% of CUR remained, a 176-fold increase compared to that with free CUR.[40] Postdigestion, CUR@CMC-Se particles expanded to an average diameter of roughly 688.5 nm (Figure S7), with a slight decrease in zeta potential but maintaining stability (−34.15 mV). This effect may be attributed to the self-assembly of CUR@CMC-Se through entropy-driven hydrophobic interactions, which create hydrophobic domains for efficient CUR encapsulation. This shielding mechanism protects CUR from degradation in the harsh gastrointestinal environment, including acidic pH and enzymatic activity. Encouraged by the high bioavailability *in vitro*, we further evaluated its bioavailability *in vivo*. As shown in Figure 1h,i, after oral administration, the fluorescence signal from CUR@CMC-Se was reduced in a time-dependent manner with a high fluorescence intensity after 48 h. All these results highlight the excellent enzymatic digestion resistance of CUR@CMC-Se, maintaining structural stability during digestion and enhancing CUR's bioavailability in the intestines.

The thermal stability of the CUR is a crucial consideration in pharmaceutical and industrial applications. Our preliminary research indicated that a 100-fold dilution of CUR ethanol solution with ultrapure water led to color disappearance after heating at 60 °C for 1 h, suggesting the instability of free CUR

https://doi.org/10.1021/acsnano.4c14373
ACS Nano XXXX, XXX, XXX−XXX

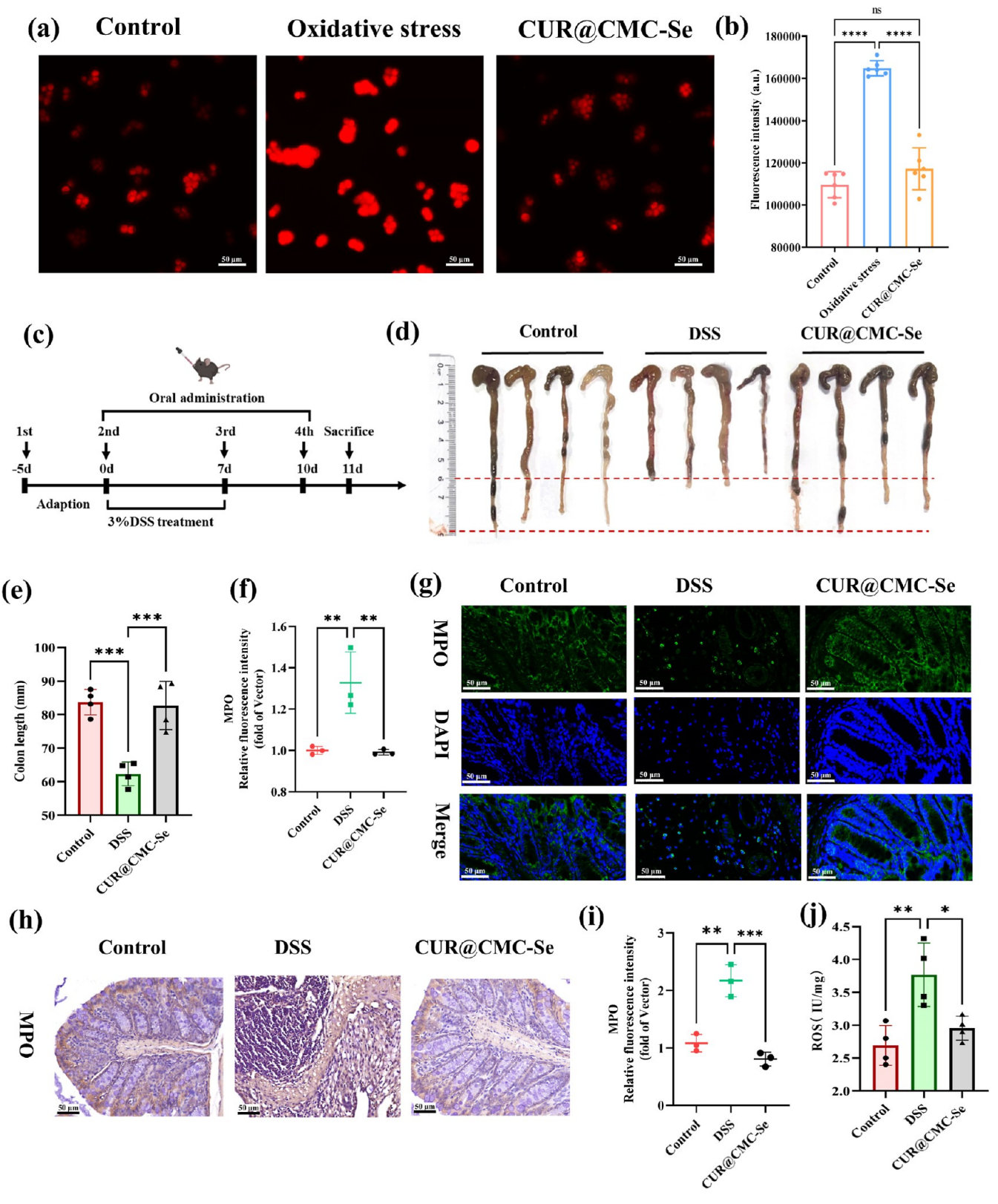

Figure 2. Colon ROS scavenging effect of CUR@CMC-Se *in vitro* and *in vivo*. (a) Intracellular ROS in HT29 cells detected by the fluorescence probe DHE and visualized under fluorescence microscopy. Scale bar: 50 μm. (b) Flow cytometry measurement of ROS levels in HT29 cells (n = 6). (c) Schematic diagram of the experimental procedure showing the treatment of DSS-induced UC mice. (d) Colon images of mice. (e) Quantitative analysis of colon length based on d (n = 4). (f,g) Quantitative analysis of mean fluorescence intensity (n = 3) and representative immunofluorescence staining images of colon sections show the expression level of myeloperoxidase (MPO). Scale bars: 50 μm. (h) Typical images of the colonic immunohistochemical staining section show the expressive extent of MPO. Scale bars: 50 μm. (i) Quantitative analysis of MPO-expressing proportion (n = 3). (j) ROS activity (n = 4) measured by ELISA.

https://doi.org/10.1021/acsnano.4c14373
ACS Nano XXXX, XXX, XXX−XXX

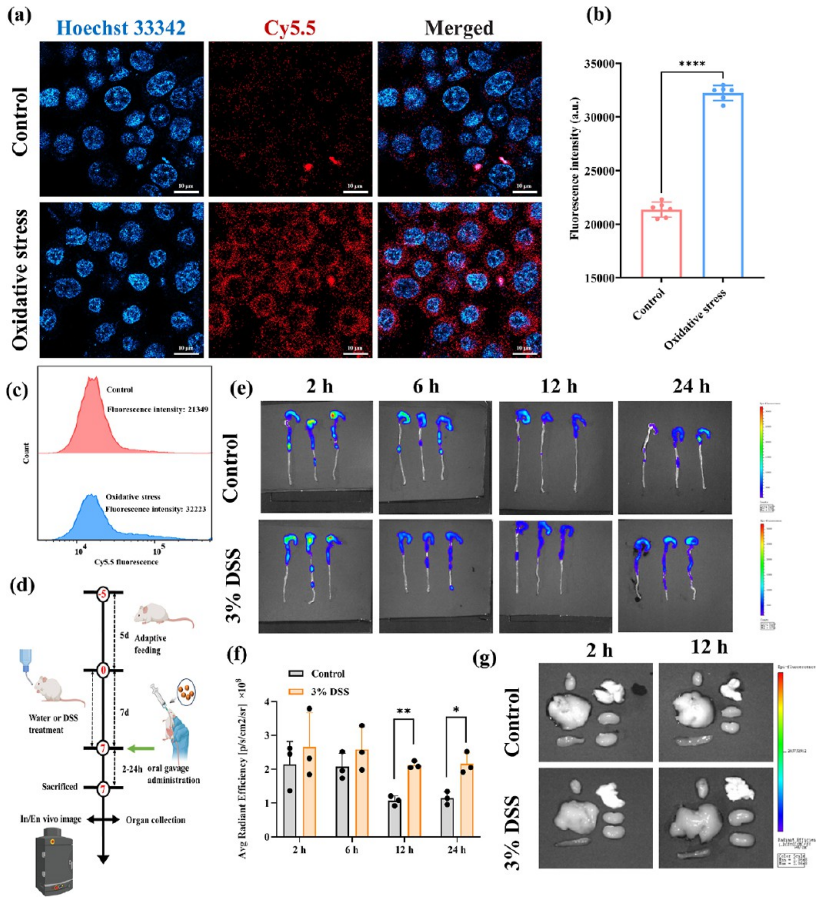

Figure 3. CUR@CMC-Se is significantly accumulated in inflamed colons. (a) Cellular uptake in HT29 cells under normal or oxidative stress, visualized *via* CLSM. Scale bar: 10 μm. (b,c) Cellular uptake behaviors of CUR@CMC-Se as quantitated by flow cytometry in normal or oxidative-stressed HT29 cells (n = 6). (d) Schematic diagram of the experimental procedure showing the *in vivo* observation of different organs collected from heathy or DSS-induced IBD mice. (e) Fluorescence imaging of colons and (f) Semiquantified analysis of the colons (n = 3). (g) Fluorescence imaging of colons, hearts, liver, spleen, lung, and kidneys (n = 3).

under thermal processing conditions.[40] In contrast, CUR@CMC-Se demonstrated an enhanced thermal stability across different temperatures. As shown in Figure S8, approximately 76% of CUR was retained after exposure to 100 °C for 1 h, highlighting its robust performance in high-temperature environments. Moreover, excellent stability was observed at 60 and 80 °C, with retention rates of 83% and 65%, respectively, after 6 h of processing, underscoring the utility of CUR@CMC-Se in processing applications. Further validation of this enhanced stability through particle size and zeta potential measurements is evident. At 100 °C, the particle size of CUR@CMC-Se gradually increased, suggesting structural expansion under these temperature conditions. This expansion led to a loss of structural integrity, which compromised its ability to protect CUR molecules effectively, resulting in leakage and degradation. Conversely, negligible changes in particle size were observed below 80 °C with a zeta potential remaining above 25 mV, indicating system stability was maintained.

Colon ROS Scavenging Effect of CUR@CMC-Se *In Vitro* and *In Vivo*. The progression of UC leads to elevated ROS levels in intestinal tissues due to sustained inflammation and immune activation, thereby aggravating the pathological condition.[41] Considering the ROS-responsive and ROS-scavenging capabilities of CUR@CMC-Se, we first examined whether CUR@CMC-Se could protect colons from oxidative stress. DHE (dihydroethidium), a common reagent for detecting ROS, was used to assess the antioxidant efficacy of CUR@CMC-Se. As depicted in Figure 2a, within the negative control group, HT29 cells exhibited a weak DHE fluorescence signal, suggesting a limited generation of ROS. On the flip side, when H_2O_2 was used to stimulate oxidative stress, a considerable increase in DHE fluorescence was observed, which pointed to a marked boost in ROS levels within the HT29 cells. After pretreatment with CUR@CMC-Se, the fluorescence diminished dramatically, suggesting that the CUR@CMC-Se still harbored CUR's antioxidant capability. The findings from the flow cytometry tallied with those of the fluorescence analysis and are depicted in Figure 2b. This evidence implies that H_2O_2 has the potential to stimulate the creation of ROS inside the cells, and CUR@CMC-Se is an effective agent in neutralizing ROS, thus shielding the HT29 cells from the adverse effects of oxidative stress caused by ROS *in vitro*.

Given the promising *in vitro* results demonstrating CUR@CMC-Se's ability to scavenge ROS, we proceeded to assess its efficacy *in vivo*. 3% dextran sulfate sodium salt (DSS) was given to mice for 7 days to build colitis models; meanwhile, the control and treated groups were given the same volume of distilled water or CUR@CMC-Se (0.5 mg/mouse/day) *via* gavage for 10 days (Figure 2c). As shown in Figure 2d,e, the colon lengths of mice in the DSS-treated group were

https://doi.org/10.1021/acsnano.4c14373
ACS Nano XXXX, XXX, XXX−XXX

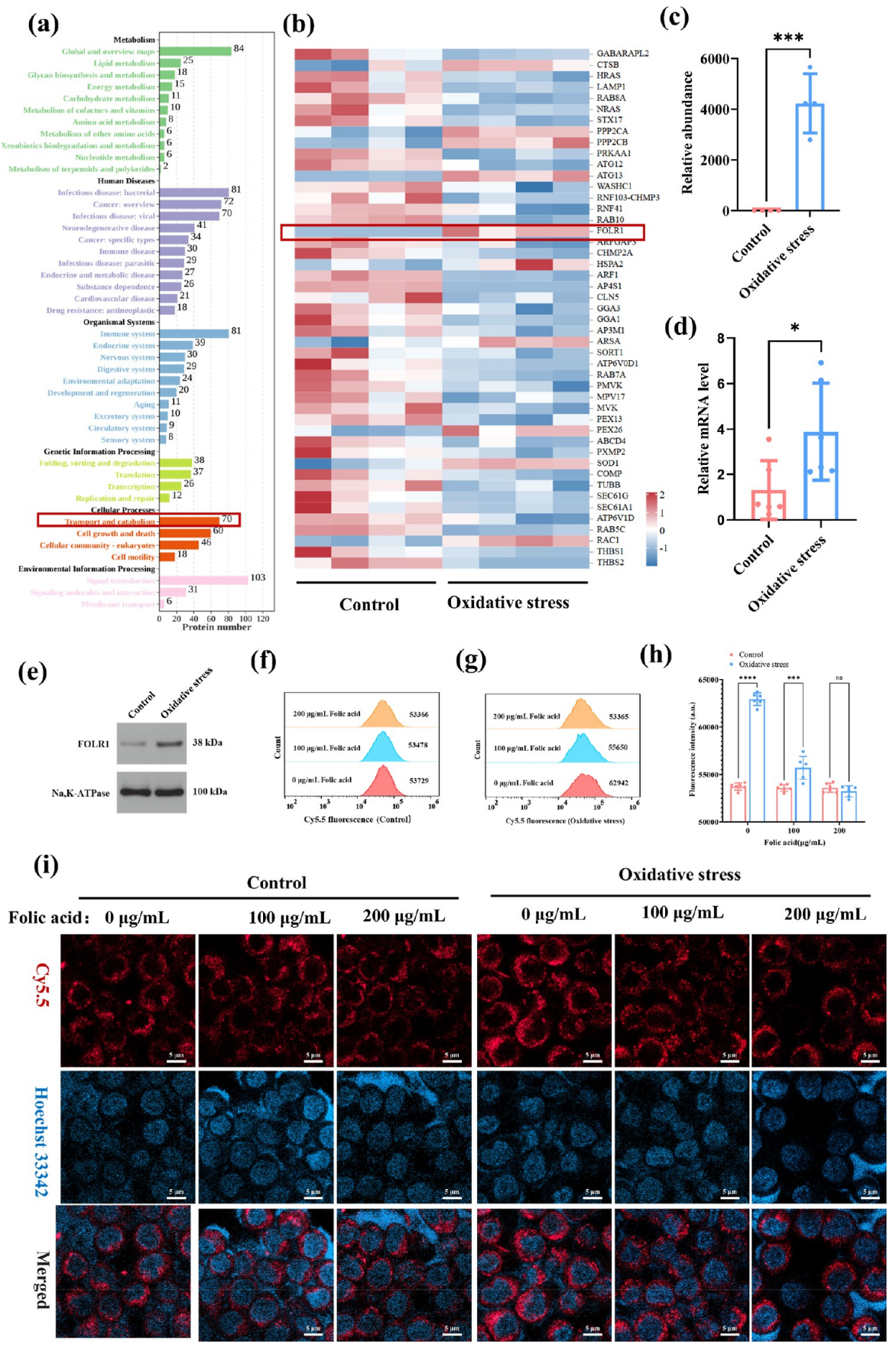

Figure 4. High expression of the folic acid receptor (FOLR1) on oxidative-stressed colon cell membranes promotes a higher cellular uptake level of CUR@CMC-Se. (a) The differential proteins between the control group and oxidative-stressed group enriched in KEGG pathways. (b) Heat maps presentation of transport and catabolism pathways based on (a). (c) Relative abundance of FOLR1 based on (b) (n = 3). (d)

https://doi.org/10.1021/acsnano.4c14373
ACS Nano XXXX, XXX, XXX−XXX

Figure 4. continued

The mRNA expression levels of FOLR1 in the membranes of HT29 cells. (e) Western blot analysis of FOLR1 in the membranes of HT29 cells. (f,g) Typical flow cytometric profiles illustrate the effect of folic acid on the cellular uptake in normal HT29 cells after treatment with CUR@CMC-Se for 6 h. (g) Typical flow cytometric profiles illustrate the effect of folic acid on the cellular uptake in oxidative-stressed HT29 cells after treatment with CUR@CMC-Se for 6 h (n = 6). (h) Quantified mean fluorescence intensities showing the effect of folic acid on the cellular uptake in normal or oxidative stressed HT29 cells after treatment with CUR@CMC-Se for 6 h (n = 6). (i) Effect of folic acid on the cellular uptake in normal or oxidative stressed HT29 cells as observed by the CLSM after treatment with CUR@CMC-Se for 6 h. Scale bar: 5 μm.

significantly lower than those of the control and CUR@CMC-Se groups, which reflected the therapeutic potential of CUR@CMC-Se. As shown in representative immunofluorescence stained sections, the colons of colitic mice showed significantly elevated expression levels of myeloperoxidase (MPO) (Figure 2f,g), which is one of the most abundant proteins expressed by neutrophils and may show adverse effects during inflammation by indirectly increasing reactive oxygen/nitrogen species (RONS) formation.[42] Encouragingly, CUR@CMC-Se could significantly alleviate the above abnormalities. Immunohistochemical staining of colonic tissues further verified the above results (Figure 2h,i). In addition, the concentration of ROS in colon tissues demonstrated that CUR@CMC-Se significantly lightened the ROS accumulation in inflamed regions (Figure 2j). Taken together, these results demonstrated that CUR@CMC-Se could indeed effectively eliminate excessive ROS within the colons.

CUR@CMC-Se Preferentially Accumulated in the Inflamed Colon. Efficient delivery of anti-inflammatory medications holds significant importance for the treatment of UC.[43] In this study, HT29, a colon cancer cell line with characteristics similar to those of colon epithelial cells, was selected to assess the cellular uptake of CUR@CMC-Se. As depicted in Figure 3a, in comparison to the control group, the oxidative-stressed cells absorbed a higher amount of CUR@CMC-Se tagged with Cy5.5, resulting in a distinctly brighter red signal within the cells. The results obtained from flow cytometry were in agreement with those from confocal imaging, as shown in Figure 3b,c. These findings clearly demonstrate that CUR@CMC-Se has the ability to target oxidatively stressed colon cells (HT29) *in vitro*. To further evaluate the colon targeting ability of CUR@CMC-Se *in vivo*, CUR@CMC-Se labeled by Cy5.5 was oral gavage administrated to healthy mice and colitis mice (Figure 3d). After sacrificing the mice, the major organs and colons were imaged to detect the localization of CUR@CMC-Se. As shown in Figures 3e, 2 after oral administration of CUR@CMC-Se, fluorescence was primarily detected in the cecum. Over time, the fluorescence signal progressively accumulated in the inflamed colon. In contrast, in control mice, the fluorescence was mainly associated with feces, indicating minimal adhesion of CMC-Se in a normal colon environment. Quantitative analysis showed that the fluorescence intensity in the DSS group was significantly higher at all time points than in the control group (Figure 3f). Notably, 12 h postadministration, the fluorescence intensity in the DSS group's colons remained high, similar to the 2 h observation, demonstrating CUR@CMC-Se's pronounced selectivity and prolonged adhesion to the inflamed colon. Additionally, *ex vivo* imaging of organs such as the heart, liver, spleen, lungs, and kidneys (Figure 3g) did not reveal any fluorescence from CMC-Se-Cy5.5, confirming its selective accumulation in the UC-inflamed colon without significant distribution to healthy tissue or other organs. These findings suggest that CMC-Se effectively enhances drug concentration and retention at the sites of the inflamed colon.

Highly Expressed Folic Acid Receptors on the Membranes of Oxidative Stressed HT29 Cells Mediated the Accumulation of CUR@CMC-Se in the Inflamed Colon. To further study why CUR@CMC-Se preferentially accumulates in the inflammatory colon, we speculated that this phenomenon may be mediated by specific transporter proteins that are highly expressed on the membranes of oxidatively stressed colon cells. Therefore, we systematically compared the expression differences of cell membrane proteins between normal and oxidatively stressed HT29 cells. A total of 1040 proteins were statistically different between normal cells and oxidative-stressed cells ($p \leq 0.05$ and fold change $\geq$1.2). Further enrichment analysis of these differentially expressed proteins revealed that 70 of the differential proteins were significantly enriched in the transport and metabolic pathways in the KEGG database (Figure 4a). The distribution of these 70 differential proteins is shown in Figure 4b, including 11 upregulated proteins (FOLR1, PPP2CB, ATG13, TUBA1C, PEX26, ARSA, SOD1, PPP2CA, RAC1, and HSPA2), among which the FOLR1 protein, as a receptor, may play an important role in endocytosis. Based on this, the potential cellular uptake mechanism of CUR@CMC-Se in oxidative stress cells may be closely related to the high expression of FLOR1 (Figure 4c). This speculation was confirmed by the significantly elevated results of qPCR and Western blot data (Figure 4d,e).

Folate receptor (FOLR1) is a membrane-bound, surface positively charged protein. Folic acid (FA) and folate conjugates bind to folate receptors with high affinity.[44] Based on this, we can competitively inhibit the function of FOLR1 by adding FA. In the FA-inhibited cell uptake experiment, we qualitatively and quantitatively compared the effects of FA on the uptake ability of normal cells and oxidative stress cells by confocal microscopy and flow cytometry analysis. As shown in Figure 4f–h, FA has no significant effect on normal cells but significantly influences the uptake of CUR@CMC-Se in oxidative-stressed cells. As the folic acid concentration increases, the average fluorescence intensity in oxidative-stressed HT29 cells decreases significantly, suggesting that the effective intracellular absorption of CUR@CMC-Se might be facilitated by the elevated expression of FOLR1 (Figure 4i). Confocal imaging shows similar trends to flow cytometry, which further confirms our conjecture. In cells, the process by which CUR@CMC-Se enters through folate receptors is a complex biophysical process. The functional component of CMC-Se, Se–NH_2, and folate acid both possess abundant amide structures that can specifically bind to folate receptors on the cell surface due to similar binding behaviors, initiating folate receptor-mediated endocytosis (Figure S9).[45] During this process, the cell membrane undergoes dynamic remodel-

https://doi.org/10.1021/acsnano.4c14373
ACS Nano XXXX, XXX, XXX–XXX

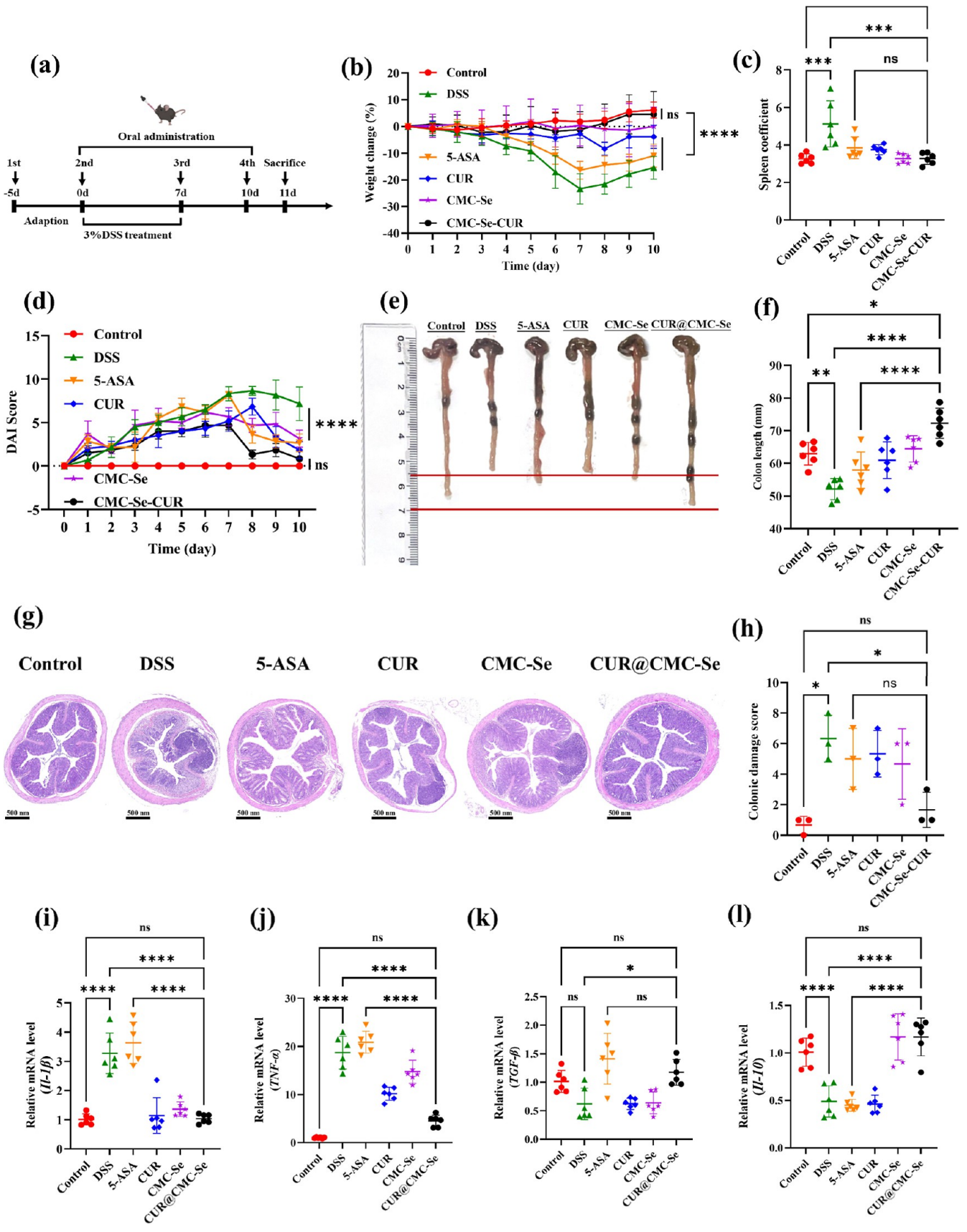

Figure 5. Preventative efficacy of CUR@CMC-Se against DSS-induced murine UC. (a) Experimental design for DSS-induced UC therapy. BALB/c mice were acclimatized for 5 days. Then, 3% DSS was administered continuously *via* drinking water for 7 days. Meanwhile, the mice were treated with PBS, 5-ASA (5 mg/mouse/day), CUR, CMC-Se, and CUR@CMC-Se (0.5 mg/mouse/day) for 10 days by oral gavage. (b) Body weight of mice (n = 6). (c) The spleen coefficient of mice after different treatments (n = 6). (d) The DAI scores of mice after the

https://doi.org/10.1021/acsnano.4c14373
ACS Nano XXXX, XXX, XXX−XXX

Figure 5. continued

treatment (n = 6). (e) Representative photographs harvested from mice after different treatments on day 11. (f) Corresponding quantified lengths of colons (n = 6). (g) H&E stained colon sections from each treatment group at day 11. (h) Histopathological scoring of colonic lesions across treatment groups (n = 3). (i–l) Colon cytokine profiles (*IL-1β*, *TNF-α*, *TGF-β*, *IL-10*) quantified by RT-qPCR at the end point (n = 6).

ing to form endocytic vesicles that encapsulate CUR@CMC-Se (Graphical Abstract).[46] The microfilaments of the cytoskeleton (primarily actin filaments) provide mechanical support for the formation and transport of endocytic vesicles through dynamic rearrangement.[46] The Rho GTPase family (including RhoC, Rac1, and Cdc42) plays a critical role by regulating cytoskeletal changes that facilitate the formation and transport of endocytic vesicles (Figure S10). Ultimately, the endocytic vesicles transport CMC-Se from the extracellular environment into the cell to exert its function. This process involves the synergistic action of multiple steps, ensuring that CMC-Se can efficiently enter the cell and perform its role.

***In Vivo* Biosafety Assessment of CUR@CMC-Se.** Ensuring biosafety is a critical requirement for a drug delivery system. To evaluate the *in vivo* safety profile of CUR@CMC-Se, mice were orally administered a dose of 25 mg/kg for 10 days (Figure S11a). Body weight measurements taken throughout the study period revealed no statistically significant difference between the treated and untreated control groups (Figure S11b). Upon completion of the trial, key organs (including heart, liver, spleen, lungs, and kidneys) and blood were harvested for comprehensive analysis. Histopathological results illustrated minor tissue damage or necrosis in CUR@CMC-Se-treated subjects (Figure S11c,d), while hematological and biochemical parameters remained within normal ranges. These findings collectively indicate excellent tissue compatibility and systemic tolerance of the CUR@CMC-Se formulation. Normal immune cell counts indicate that CUR@CMC-Se did not trigger abnormal immune responses in mice (Figure S11e). The whole blood and serum biochemistry analysis showed that CUR@CMC-Se-treated mice were consistent with the control mice (Figure S11f), further confirming the excellent biocompatibility of CUR@CMC-Se *in vivo*. In summary, CUR@CMC-Se did not exhibit significant adverse effects on the organ structure and function in mice, did not induce excessive immune responses, and demonstrated good biocompatibility and safety, rendering it an efficient and secure drug delivery platform.

Preventive Effects of CUR@CMC-Se in DSS-Induced Colitis Mice. Encouraged by the excellent antioxidant properties of CUR@CMC-Se and its capability for ROS-responsive targeted drug release in the inflamed colon, it shows promise for the clinical treatment of UC. To assess the preventive efficacy, we established a DSS-induced model in mice (Figure 5a). Notably, DSS-treated mice demonstrated significant body weight reduction and hematochezia at the early stage of model establishment with no significant improvement in UC symptoms by day 10 (Figure 5b). Subsequently, we calculated the DAI scores for each mouse based on fecal and occult blood scoring (Figure 5d). The results revealed that the DAI scores of DSS-treated mice showed an increasing trend in the initial days, with a turning point occurring on day 7. After the cessation of DSS administration on day 7, the DAI scores of mice in all groups decreased, whereas the DAI score in the DSS group continued to rise, indicating that drug intervention during DSS-induced modeling effectively alleviated inflammation in the mice. Moreover, the spleen coefficient results (Figure 5c) indicated a reduction in inflammation following drug intervention. Anatomical results (Figures 5e,f, S12) showed significant restoration of colon length in the CUR@CMC-Se group, while other DSS-treated mice exhibited varying degrees of colon shortening. This suggests that while other treatments alleviated UC symptoms, they did not restore the colon to a healthy state. H&E staining analysis revealed extensive inflammatory infiltration, crypt structure atrophy, and severe intestinal damage in the colons of DSS, CUR, and CMC-Se groups. In contrast, significant improvements in colon conditions were observed in mice treated with 5-ASA and CUR@CMC-Se (Figures 5g,h, S13). Intestinal barrier damage is a major pathological feature of the UC. ZO-1, an essential tight junction protein on epithelial cell membranes, plays a crucial role in maintaining intestinal health. We analyzed ZO-1 expression using immunohistochemical methods. Figure S14 shows that ZO-1 expression in goblet cell membranes was significantly reduced and discontinuous in the DSS group, indicating disrupted intercellular connections and functional abnormalities. In contrast, ZO-1 expression significantly increased in all groups, except the CMC-Se group. ZO-1 expression in the 5-ASA and CUR groups was restored to levels similar to those of the control group, although gaps in ZO-1 distribution on the cell membranes remained, indicating incomplete restoration of tight junctions. The CUR@CMC-Se group demonstrated a uniform and continuous distribution of ZO-1 in goblet cell membranes. Immunohistochemical staining results suggest that CUR@CMC-Se enhances ZO-1 expression and tight junction integrity, contributing to intestinal barrier repair and health restoration. Additionally, the anti-inflammatory effects of CUR@CMC-Se were noted. RT-qPCR analysis (Figure 5i–l) showed that CUR@CMC-Se effectively inhibited the expression of pro-inflammatory factors TNF-α and IL-1β, reducing inflammation and tissue damage, while increasing the expression levels of anti-inflammatory factors IL-10 and TGF-β, thereby enhancing anti-inflammatory effects and promoting intestinal repair and inflammation alleviation. Overall, CUR@CMC-Se demonstrates significant preventive intervention effects in the UC mouse model, effectively reducing symptoms and improving intestinal barrier function.

Therapeutic Effect of CUR@CMC-Se in DSS-Induced Colitis Mice. In the study of preventive effects, we observed that CUR has a significant effect on suppressing inflammation. This provides strong evidence of the potential of CUR@CMC-Se as a preventive therapeutic approach. However, in actual clinical applications, treating existing inflammation is the primary goal of drug development. Here, we employed a pretreatment model to comprehensively evaluate the therapeutic effects of CUR@CMC-Se in a UC mouse model (Figure 6a). As shown in Figure 6b–e, CUR@CMC-Se continues to exhibit effectiveness in maintaining mouse body weight, reducing DAI scores, and restoring colon length. In contrast, other treatment groups showed decreased efficacy compared to preventive treatment. Notably, as seen in Figure

https://doi.org/10.1021/acsnano.4c14373
ACS Nano XXXX, XXX, XXX–XXX

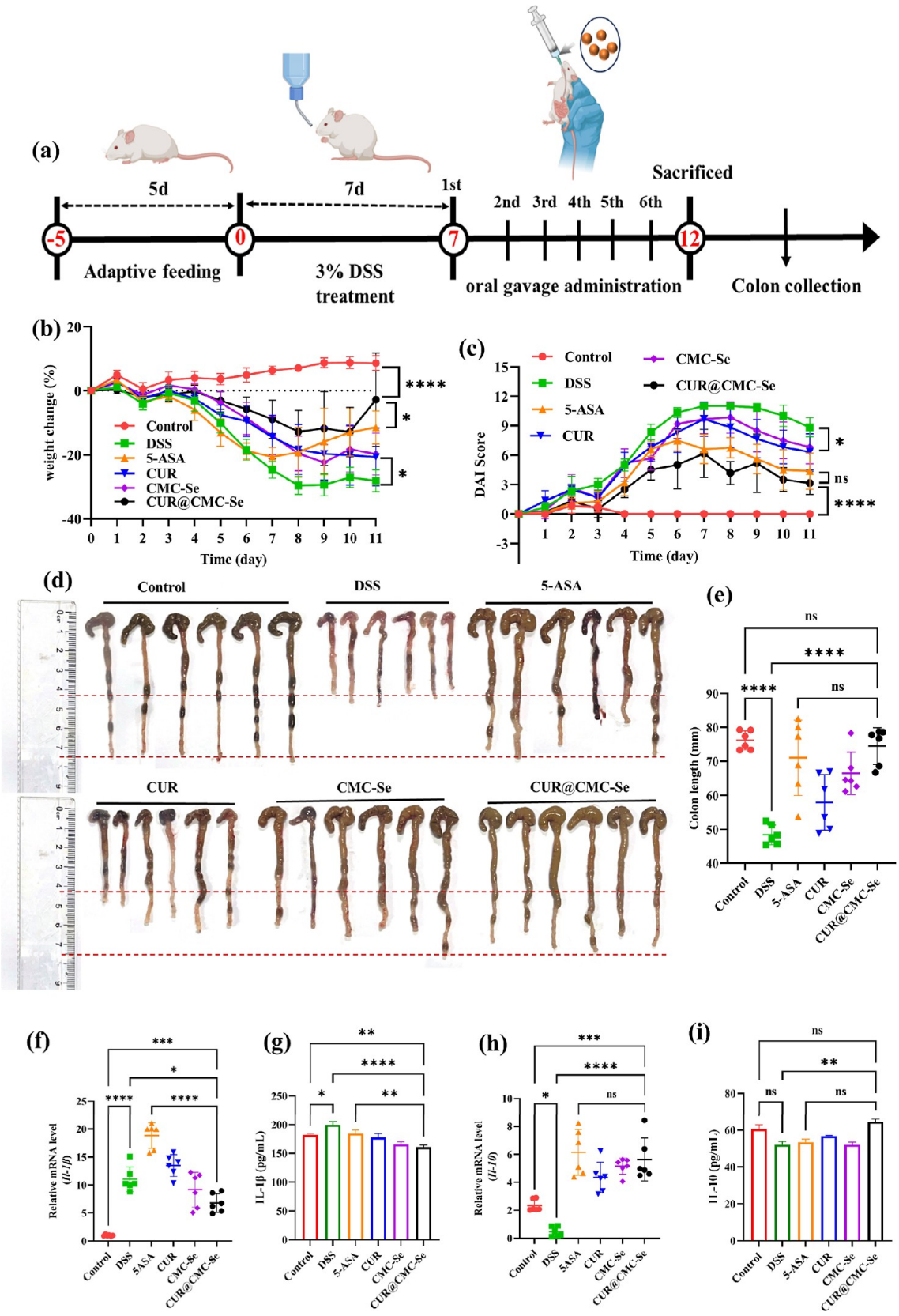

Figure 6. Treatment efficacy of CUR@CMC-Se against DSS-induced murine UC. (a) Treatment protocol for ulcerative colitis mice. BALB/c mice were acclimatized for 5 days. Then, the mice were fed 3% DSS for 7 days. Thereafter, the mice were treated with PBS, 5-ASA (5 mg/mouse/day), CUR, CMC-Se, and CUR@CMC-Se (0.5 mg/mouse/day) for another 5 days by oral gavage. (b) Body weight change of mice (n = 6). (c) The DAI scores of mice after the treatment (n = 6). (d) Representative photographs harvested from mice after different treatments on day 13 (n = 6). (e) Corresponding quantified lengths of colons (n = 6). (f–i) The levels of IL-1β and IL-10 in the colon tissues measured by RT-qPCR and ELISA.

https://doi.org/10.1021/acsnano.4c14373
ACS Nano XXXX, XXX, XXX−XXX

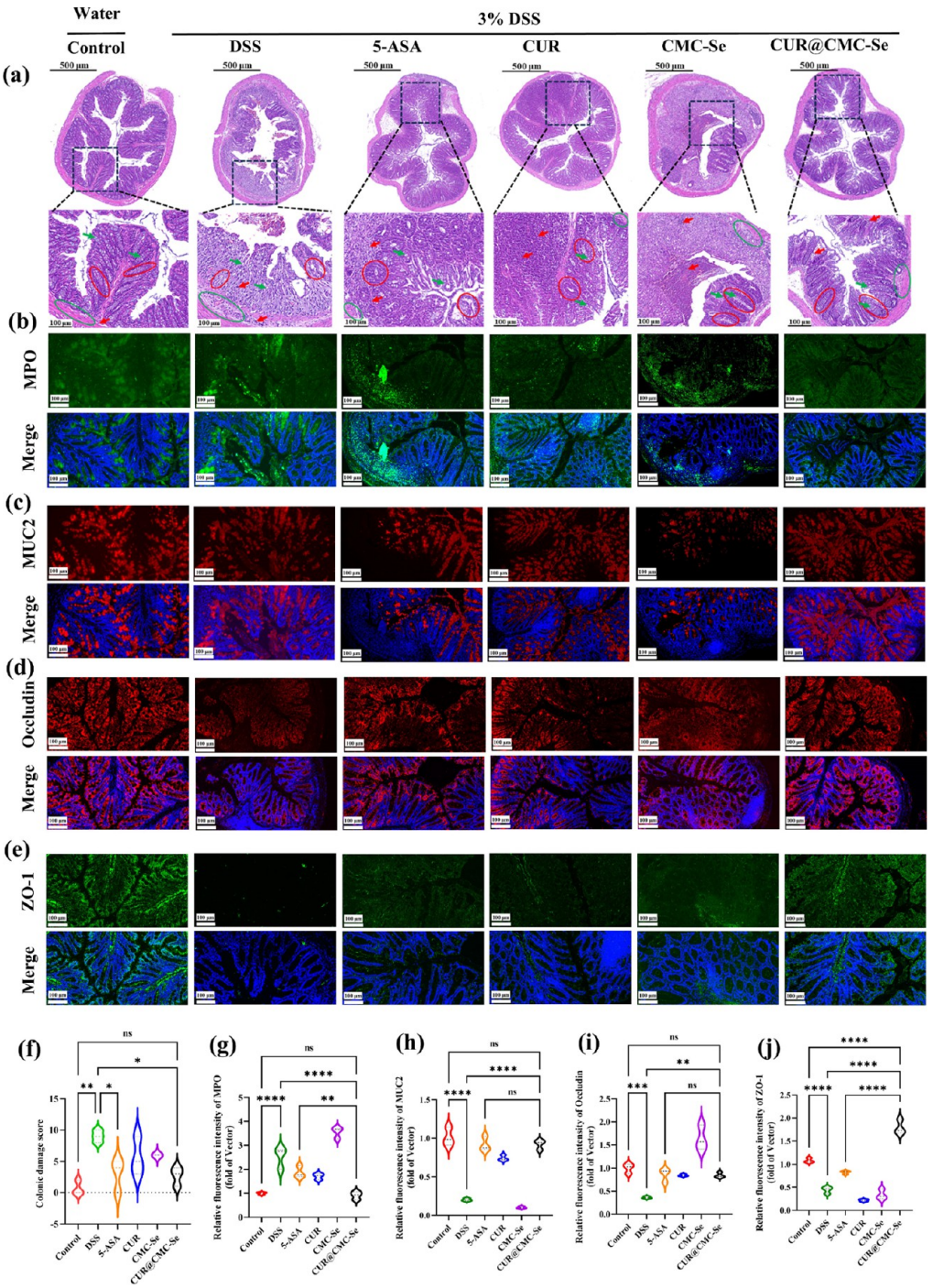

Figure 7. Repair effect of CUR@CMC-Se against DSS-induced intestinal barrier damage. (a) H&E-stained colon sections from treatment groups at day 13 (n = 3 biological replicates). Immunofluorescence staining images of colonic sections show the expression level of (b) MPO, (c) MUC2, (d) Occludin, and (e) ZO-1. Scale bars: 100 μm. (f–j) Quantitative analysis based on the mean fluorescence intensity of a–e (n = 3). The red arrows indicate neutrophils, the green arrows indicate goblet cells, the red circles highlight crypts, and the green circles indicate the inflammatory status of the mucosal muscle and submucosa.

6d, except for the control and CUR@CMC-Se groups, colon length recovery in the other groups was unstable, with significant variability between samples, and only a few individuals showed recovery to the control level. Interestingly, the commonly used positive control drug 5-ASA also showed good recovery capabilities; however, some mice displayed poor growth conditions during rearing, and overall UC symptoms did not improve, as reflected in the significantly shortened colons of two mice. This may be due to organ toxicity from 5-ASA in weakened mice, leading to inadequate overall recovery. In contrast, CUR@CMC-Se consistently and effectively improved symptoms (body weight changes, DAI score changes, and restored colon length) in both models.

During intestinal tissue inflammation, harmful microorganisms damage intestinal epithelial cells, leading to mucosal erosion and increased intestinal permeability.[47] This process allows pathogens to enter the spleen through the circulatory system, activating immune cells, such as macrophages and

https://doi.org/10.1021/acsnano.4c14373
ACS Nano XXXX, XXX, XXX–XXX

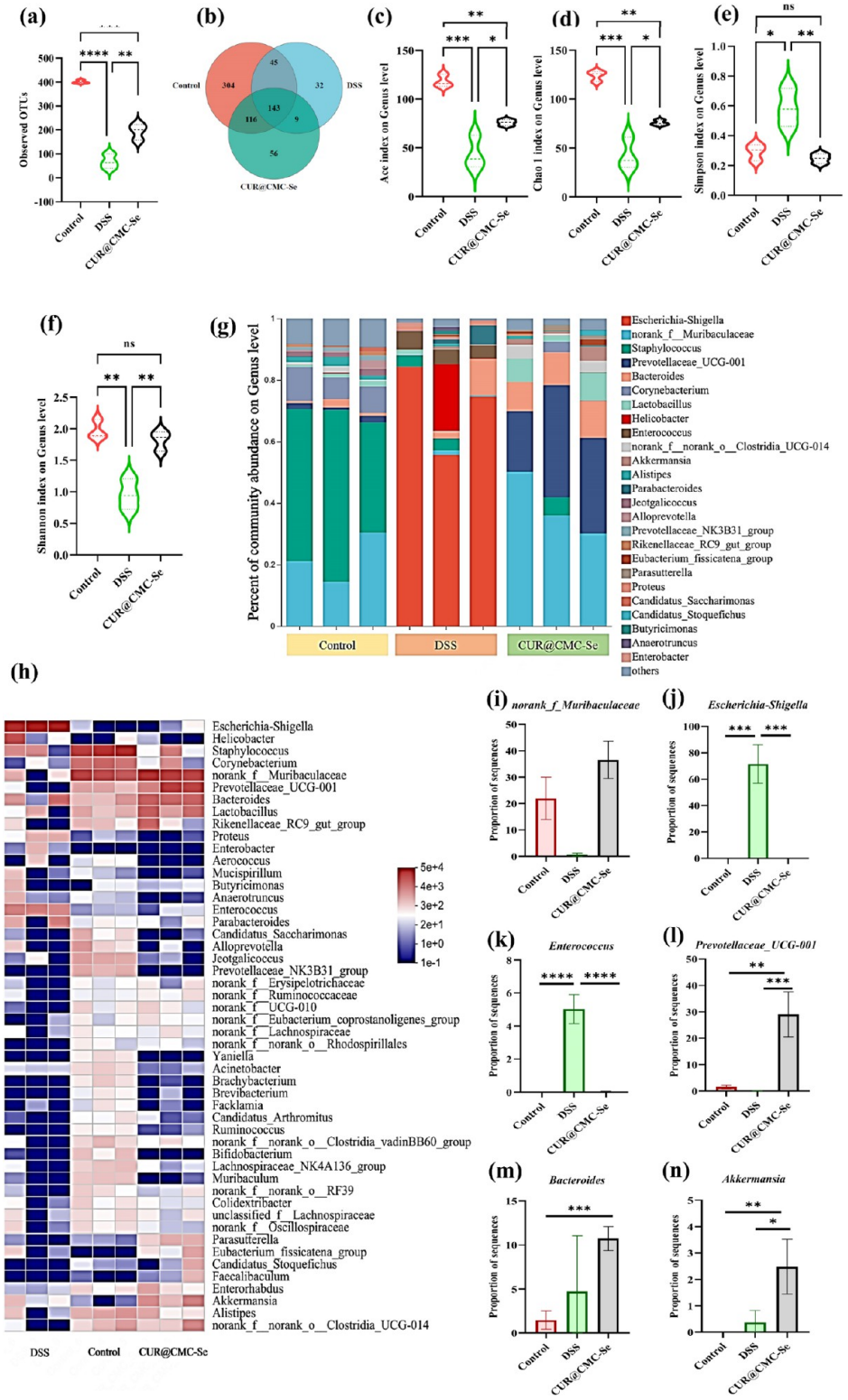

Figure 8. Modulation of gut bacteria by CUR@CMC-Se during colitis treatment. Comparison of alpha diversity assessed by (a) observed OTUs, (b) Venn diagram, (c) Ace index, (d) Chao 1 index, (e) Simpson index, and (f) Shannon index. (g) Column diagram of the relative abundance of the gut microbiome at the genus level. (h) Heatmap illustration of gut microbial distribution at the genus level. Relative abundance of *norank_f_Muribaculaceae* (i), *Escherichia-Shigella* (j), *Enterococcus* (k), *Preotellaceae_UCG-001* (l), *Bacteroides* (m), and *Akkermansia* (n).

neutrophils. Subsequent inflammatory mediator release stimulates adaptive immune responses (T/B cell activation), perpetuating an inflammatory cascade that compromises intestinal barrier integrity.[48] Both qPCR and ELISA analyses (Figures 6f,g, and S15a) demonstrated markedly elevated expression of pro-inflammatory mediators (IL-1β and TNF-α) at transcriptional and protein levels in DSS-treated mice, whereas CUR@CMC-Se markedly reduced the contents of IL-

https://doi.org/10.1021/acsnano.4c14373
ACS Nano XXXX, XXX, XXX−XXX

1β and TNF-α, suggesting that CUR@CMC-Se could inhibit the expression of pro-inflammatory cytokines. Notably, IL-10, a multifunctional anti-inflammatory cytokine, has been shown in previous studies to reduce the production of inflammatory mediators by inhibiting pro-inflammatory signaling pathways.[49] We subsequently assessed the levels of several inflammation-related factors directly or indirectly regulated by IL-10 in the colon.

As illustrated in Figures 6h,i, and S15b,c, CUR@CMC-Se markedly reduced the contents of IL-10, IL-6, and TGF-β, showing reductions of 1.22-fold, 3.03-fold, and 1.8-fold, respectively, compared to the DSS group, thereby effectively mitigating inflammation. Taken together, CUR@CMC-Se might exert a therapeutic effect on UC by inhibiting pro-inflammatory factors, up-regulating anti-inflammatory factors, and facilitating the restoration of colonic structure.

Repair Effect of CUR@CMC-Se on UC-Induced Intestinal Barrier Dysfunction. Repair of the intestinal barrier is also a critical parameter for evaluating the efficacy of CUR@CMC-Se treatment. Histological analysis (Figure 7a) revealed that DSS-induced intestinal inflammation caused more severe damage than simultaneous modeling and intervention. The DSS, CUR, and CMC-Se groups exhibited extensive areas of inflammatory infiltration, with significant crypt architectural distortion and near-complete loss of goblet cells. However, treatment with 5-ASA or CUR@CMC-Se led to notable improvements in colonic pathology, as evidenced by significantly reduced histopathological scores (Figure 7f), indicating the amelioration of intestinal damage.

Furthermore, immunofluorescence stained sections of colonic tissues indicated that CUR@CMC-Se could significantly restore the expression of MPO to a normal level, evidencing that CUR@CMC-Se could effectively prevent the impending oxidative damage attributed to colitis (Figure 7b,g).

The proteins associated with tight junctions (Occludin and ZO-1) and mucus (MUC2) are key proteins crucial for maintaining the intestinal epithelial barrier and preventing harmful substances from penetrating the intestinal wall. Immunofluorescence staining and quantitative analysis were employed to evaluate these proteins. As shown in Figure 7c–e, DSS treatment markedly reduced the expression of these proteins, indicating compromised tight junction integrity within the intestinal epithelial environment. Treatment with CUR@CMC-Se effectively increased MUC2, Occludin, and ZO-1 expression, showing no significant differences compared to the control group. Additionally, the therapeutic efficacy of CUR@CMC-Se was comparable to or even better than that of 5-ASA (Figure 7h–j). Notably, CMC-Se demonstrated a unique capacity to specifically enhance Occludin secretion (Figure 7i), suggesting a synergistic effect between CMC-Se and CUR during the treatment. In conclusion, CUR@CMC-Se significantly improves the intestinal barrier integrity and pathology in DSS-induced colitis.

CUR@CMC-Se Modulates the Gut Microbiome Disorder Caused by DSS. The gut microbiota is essential for intestinal homeostasis and immune regulation.[50] α-Diversity metrics evaluate microbial community richness and diversity within samples. As illustrated in Figure 8a–f, compared to healthy mice, DSS-induced colitis in mice resulted in a significant reduction in microbial diversity and abundance, with the number of unique gut microbial species decreasing to 32 (Figure 8b). The Chao 1 index and Shannon index dropped from 124.04 and 1.973 to 42.77 and 1.089, respectively. CUR@CMC-Se can effectively restore microbial diversity; the Chao 1 index increased to 75.72, and the number of unique microbial species rose to 56. This indicates a significant improvement in both the Chao 1 index and Shannon index, with the latter returning to levels comparable to that of the control group, showing no significant statistical differences. Further analysis of the community composition revealed differences in gut microbiota across different groups. *Muribaculaceae*, an important intestinal bacterium, promotes the growth of beneficial bacteria and inhibits harmful bacteria through its metabolic activities, such as short-chain fatty acids (SCFAs) synthesis, thus maintaining intestinal microbial balance.[51] As shown in Figure 8i, the abundance of *Muribaculaceae* in the gut of UC mice nearly disappeared, with pathogenic *Escherichia-Shigella* becoming predominant. This suggests that shifts in the dominant gut microbiota appear to be intricately associated with the onset of intestinal inflammation. Oral administration of CUR@CMC-Se not only suppressed the abundance of pathogenic *Escherichia-Shigella* but also restored *Muribaculaceae* levels. Analysis of SCFAs in the gut revealed that the DSS treatment group had significantly reduced levels of predominant SCFAs, including acetate, propionate, butyrate, isobutyrate, and isovalerate ($p < 0.05$). In contrast, CUR@CMC-Se treatment facilitated the regeneration of these SCFAs, with concentrations increasing from 25.76, 16.01, 14.19, 6.4, and 7.26 to 73.38, 39.72, 41.79, 32.51, and 35.34, respectively (Figure S16). This effect may be attributed to CUR@CMC-Se's regulation of SCFA-producing microbiota (*Muribaculaceae* and *Bacteroidota*).

Generally, acetate, propionate, and butyrate play critical roles in activating intestinal cells and maintaining mucosal integrity and overall gut health. They contribute to enhancing the mucosal barrier function and reducing the permeability of harmful substances, thus protecting the intestine from inflammation and damage.[52] Additionally, CUR@CMC-Se increased the abundance of bacteria such as *Prevotellaceae_UCG-001* (Figure 8l), which has dual effects, both anti-inflammatory and potential for immune dysregulation. However, an increase in *Prevotellaceae_UCG-001* generally indicates a beneficial outcome.[53] Notably, the abundance of *Akkermansia*, a bacterium of increasing scientific interest, also rose significantly (Figure 8n). *Akkermansia* abundance is often positively correlated to mucosal layer thickness. Higher *Akkermansia* levels aid in increasing mucus secretion, thus enhancing the intestinal barrier function.[54] Unlike other bacteria, *Akkermansia* feeds on mucin in the mucosal layer rather than relying on external nutrients. During UC, reduced food intake and decreased carbohydrate levels result in a significant reduction of nonmucin-consuming species. *Akkermansia* specifically degrades mucin to produce acetate, propionate, and ethanol, modulating host immune responses and lipid metabolism while providing energy for other bacteria's colonization. Mucin degradation prompts the host to produce more mucin, maintaining the dynamic balance of these proteins.[55] Recent studies have shown that *Akkermansia* supplementation increases the colonic mucus layer thickness approximately 3-fold, a notable improvement compared to increases induced by beneficial *Lactobacillus* strains.[55] Additionally, *Akkermansia* can activate the TLR2 pathway through AMPK signaling, altering the expression of tight junction proteins Occludin and ZO-1, thus regulating intestinal permeability and aiding in the repair of damaged gut barriers, consistent with our findings.[56] Therefore, one of the

https://doi.org/10.1021/acsnano.4c14373
ACS Nano XXXX, XXX, XXX−XXX

mechanisms by which CUR@CMC-Se treats UC may involve enhancing the abundance of beneficial bacteria that produce SCFAs and increasing the mucus layer thickness, ultimately aiding in the restoration of intestinal health and reducing inflammation.

DISCUSSION

Ulcerative colitis (UC) is a chronic inflammatory bowel disease primarily affecting the colonic mucosa, often extending to the rectum and deeper intestinal layers, leading to significant morbidity and reduced quality of life for affected individuals.[57] The overproduced ROS, damage to the intestinal mucosal barrier, and dysbiosis of gut microbiota are critical pathogenic foundations of UC.[58] Elevated ROS levels during colitis progression create a vicious cycle by (1) activating inflammatory cells to generate additional ROS, exacerbating epithelial damage, (2) suppressing commensal microbiota colonization, and (3) disrupting mucosal microenvironment homeostasis.[59] In our work, intestine-targeted polymer CMC, which is resistant to gastric fluid digestion and can swell in the intestines, was modified with a ROS-responsive fragment (Se−Se) and applied to encapsulate CUR (CUR@CMC-Se) to scavenge excessive ROS and protect colons from oxidative damage. Our results demonstrated that the CUR@CMC-Se with ROS-responsive and ROS scavenging capability can effectively scavenge elevated ROS within the inflamed colon, alleviating colitis symptoms (Figures 1 and 2).

Targeted drug delivery that responds to the pathological microenvironment offers new opportunities to minimize off-target systemic side effects and improve the therapeutic efficacy of treatments for UC. The inflamed colon is characterized by a high concentration of positively charged proteins and elevated levels of ROS.[60] Previous studies found that negatively charged systems, such as liposomes, gold nanoparticles, hydrogels, and nanoparticles, exhibit higher delivery efficiency to inflammatory regions than neutral or positively charged systems.[61−63] This may be due to the fact that during the inflammatory response, numerous inflammatory mediators, such as TNF-α, IL-1β, and MPO secreted by neutrophils, are positively charged and contain abundant positively charged amino acids.[64,65] These positively charged proteins can interact with negatively charged nanoparticles through electrostatic attraction (Graphical Abstract), promoting preferential accumulation of the systems in the inflammatory region.[66] Ideally, our CUR@CMC-Se nanoparticles also possess a strong negative zeta potential and demonstrate similar preferential accumulation in inflamed colon areas. At the same time, the overproduced ROS at the inflamed area stimulates the cleavage of CMC-Se and synchronously releases the encapsulated CUR in situ to scavenge excessive ROS. The results demonstrated that the detained CUR@CMC-Se elevated the gathering of CUR at the colitic area, which was mediated by the high expression levels of folic acid receptors on the membranes of oxidative stressed HT29 cells, helping balance oxidative stress and protecting the damaged intestinal barrier from graver injury (Figures 3, 4, and 7).

The imbalance of intestinal flora, primarily marked by significant changes in the ratios of normal flora species, can impact the occurrence and progression of UC through various pathways, including enteric microbial factors, aberrant immune responses, and a compromised intestinal mucosal barrier.[67] Our smart ROS-responsive nanocarrier enabled the targeted release of CUR into the gut, especially in inflammatory areas. This was due to the high expression of the folic acid receptor on the membrane of oxidative-stressed colon cells, which mediated the internalization of CUR@CMC-Se. CUR was capable of scavenging excessive ROS, while CMC-Se had the ability to enhance the retention of CUR in the colon. In addition, the CMC could be broken down and metabolized by microflora, thereby regulating the intestinal microenvironment and selectively enriching beneficial bacteria while suppressing pathogenic species. This microbiome remodeling contributed to the therapeutic efficacy of CUR@CMC-Se in alleviating DSS-induced colitis (Figure 8). Notably, CUR@CMC-Se treatment restored near-normal physiological parameters, including body weight, MPO activity, colon length, spleen weight, histopathology, and cytokine profiles, comparable to those of healthy controls (Figures 5 and 6).

CONCLUSIONS

To summarize, we developed a curcumin-loaded nanoparticle (CUR@CMC-Se) featuring ROS-responsive behavior through diselenide bonding. This innovation enabled targeted and controlled curcumin release to effectively treat UC. Both *in vitro* and *in vivo*, CUR@CMC-Se demonstrated outstanding ROS-neutralizing and ROS-responsive characteristics. The nanocarrier was readily absorbed by HT29 cells and, when administered orally, showed preferential accumulation in the inflamed colon tissue. In colitis models, CUR@CMC-Se successfully mitigated UC symptoms by restoring oxidative balance, repairing intestinal barrier integrity, and modulating gut microbiota composition. With its proven biocompatibility, this platform not only offers a promising UC treatment but also serves as a versatile drug delivery system that could be adapted for other anti-inflammatory therapies.

METHODS

Synthesis and Characterization of Se−NH_2. Prior to the synthesis of carboxymethyl cellulose-selenium, an ROS-responsive element was prepared using the following method. Initially, 2,2′-diselanediyldiethanamine dihydrochloride (5 g, 0.016 mmol) was dissolved in 100 mL of dimethylacetamide (DMF) at 0 °C with stirring for 10 min. Once fully dissolved, 5.7 mL of *N*-methyl morpholine was added and stirred for an additional 5 min. Next, *N*-α-phthalimido methyl-*N*-epsilon-*t*-butyloxycarbonyl-D-lysine (17.82 g, 0.038 mmol) was added, and the mixture was agitated for 10 min. Subsequently, 1-hydroxyphenylpropanetriazole (2.332 g, 0.0173 mmol) and 1-ethyl-3-(3-(dimethylamino)propyl) carbodiimide (EDC) (9.933 g, 0.052 mmol) were introduced into the mixture. After 20 min of continuous stirring, the reaction was conducted overnight under ambient conditions.

Upon completion of the reaction, the contents were moved to a separatory funnel, and then, an ethyl acetate and water blend was introduced for the extraction process. The organic layer from the top was carefully separated, and the remaining aqueous phase underwent three successive extractions with fresh ethyl acetate. After all of the organic fractions were pooled, the solution was transferred to a rotary evaporator (100 rpm, 4 °C) to remove the organic solvent. The resulting residue was washed twice with a saturated sodium chloride solution to remove impurities, followed by the addition of anhydrous sodium sulfate to remove water. For further purification, recrystallization was performed. Methanol was added to the product until it was fully dissolved, and then, an appropriate amount of dichloromethane was added until the solution became turbid. The mixture was left at 25 °C for 24 h, allowing crystals to form. The light-yellow solid obtained, identified as Se-NHBoc, was filtered and dried.

The purified Se-NHBoc was dissolved in dichloromethane until fully dissolved and then reacted for 6 h with an additional 4-fold volume of trifluoroacetic acid. Ultimately, sodium bicarbonate's

https://doi.org/10.1021/acsnano.4c14373
ACS Nano XXXX, XXX, XXX−XXX

saturated solution was introduced to neutralize any residual trifluoroacetic acid. The resulting product, named Se−NH_2, was filtered, dried, and stored at 4 °C. The chemical structure was confirmed by ^{1}H NMR.

Synthesis of CMC-Se. To prepare CMC-Se, a solution was first created by dissolving 2 g of CMC in 450 mL of 50 mM MES buffer (pH 5.5), supplemented with 50 mL of DMSO to ensure full dissolution over 12 h. Subsequently, a 50 mM solution of *N*-hydroxysuccinimide (NHS) and a 100 mM concentration of 1-ethyl-3-(3-(dimethylamino)propyl) carbodiimide hydrochloride (EDC) were blended into the CMC solution, and the mixture was vigorously stirred for 2 h. Concurrently, Se−NH_2 (100 mg) was dissolved in a 10 mL solvent that was identical to the composition of the CMC solution, and this solution was then meticulously added to the CMC solution drop by drop. The chemical process was continuous for 24 h at ambient temperature. Postreaction, the raw material was placed in a dialysis bag using the dialysis method (M_W cutoff: 10 kDa) and purified against ultrapure water over 3 days, with the water replaced every 4 h to eliminate residual low molecular weight impurities. Finally, the purified material was lyophilized for 3 days, yielding a light-yellow fibrous solid, identified as CMC-Se.

H_2O_2 was chosen as a representative of the ROS to study the oxidation behavior of CMC-Se. In short, CMC-Se was dissolved at a concentration of 10 mg/mL in PBS buffer (pH 6.8) containing 10 mM H_2O_2, incubated for 36 h, and freeze-dried for testing.

Preparation and Characterization of CUR@CMC-Se. For the preparation of CUR@CMC-Se, CMC-Se and CUR were dissolved in deionized water and acetone at concentrations of 10 mg/mL, respectively. 1 mL of CUR acetone solution was added to 10 mL of CMC-Se solution and ultrasonicated for 10 min (20.6235 kHz, 340 W, 5 s on and 3 s off of interval), and then, the sample was transferred to a high-pressure PhD homogenizer for pretreatment for 6 cycles at 5000 psi, followed by homogenization for 6 cycles at 20,000 psi, and finally homogenization for 6 cycles at 30,000 psi. After homogenization, the acetone was removed under a vacuum at 40 °C until completely evaporated. The sample was then centrifuged (3000 rpm, 5 min) to yield uniformly dispersed curcumin-loaded nanoparticles, designated as CUR@CMC-Se. To determine the maximum curcumin loading capacity, absorbance measurements were taken at 425 nm by using an ultraviolet spectrophotometer. Curcumin concentrations were quantified based on the standard calibration curve as follows

$$Y = 0.1546X + 0.0045 (R^2 = 0.999) \quad (1)$$

where X is the curcumin concentration (μg/mL) and Y is the absorbance at 425 nm; the linear range of X is 1.5−9 μg/mL.

The loading rate of the nanoparticles to curcumin was calculated according to the following equation

$$\text{Loading rate}(\%,\text{w/w}) = \text{loading amount of curcumin}/\text{amount of nanoparticles} \times 100 \quad (2)$$

X-ray Photoelectron Spectrometry (XPS) Analysis. The Se-bond energy was measured via XPS. CMC-Se samples, both untreated and those exposed to 10 mM H_2O_2 for 36 h, were placed on the sample holder. After loading into the instrument's chamber, the samples were transferred to the analysis compartment once the pressure dropped below 2.0×10^{-7} mbar. Measurements were conducted with a 400 μm spot size, an operating voltage of 12 kV, and a filament current of 6 mA. For broad-spectrum analysis, a 150 eV pass energy and a 1 eV step size were applied, while high-resolution scans used a 50 eV pass energy with 0.1 eV increments.

Determination of Selenium Content and Distribution of CMC-Se. 85 mg of CMC-Se solid was subjected to acid dissolution pretreatment, and after treatment, the selenium content in the sample was determined using inductively coupled plasma optical emission spectroscopy.

The distribution and mass proportion of selenium elements were determined by energy-dispersive X-ray Spectrometry (EDX) using TEM.

Particle Size and Zeta Potential Measurement. The mean particle size, polydispersity index (PDI), and zeta potential of CMC-Se (with or without 10 mM H_2O_2 for 36 h) and CUR@CMC-Se (with or without 10 mM H_2O_2 for 36 h) at various time points were obtained using a particle size analyzer. Samples were diluted with ultrapure water and measured at 25 °C. Each measurement was repeated three times.

ATR-FTIR Analysis. The molecular composition of curcumin powder, as well as blends containing curcumin mixed with CMC-Se, CMC-Se alone (both with and without exposure to 10 mM H_2O_2 for 36 h), and CUR@CMC-Se (also with and without 10 mM H_2O_2 treatment for 36 h), was examined using ATR-FTIR spectroscopy. The analysis was performed with a PerkinElmer Universal ATR attachment featuring a diamond crystal. Samples were evaluated in the transmittance mode under the following parameters: a spectral window spanning 4000 to 550 cm^{-1}, 32 accumulated scans, and a resolution of 4 cm^{-1}.

Different Scanning Calorimetry (DSC) Analysis. The thermal behaviors of curcumin powder, a mixture of curcumin and CMC-Se, CMC-Se (with or without 10 mM H_2O_2 for 36 h), and CUR@CMC-Se (with or without 10 mM H_2O_2 for 36 h) were evaluated using a differential scanning calorimeter. The sample was encased within a sleek aluminum plate, with a temperature range spanning from a frigid 30 °C to a blistering 600 °C. It was heated up at a steady clip of 10 °C/min and was maintained in a nitrogen flow at a moderate rate of 20 mL/min.

Observation of Morphology. The morphology of CMC-Se (with or without 10 mM H_2O_2 for 36 h) and CUR@CMC-Se (with or without 10 mM H_2O_2 for 36 h) were examined by TEM and SEM.

***In Vitro* Drug Release.** To investigate the oxidation behavior of CUR@CMC-Se in vitro, CUR@CMC-Se (1 mg/mL) was initially incubated in PBS buffer at pH 1.2 for 2 h. Subsequently, the pH was adjusted to 6.8 and different volumes of H_2O_2 were added to make the content of the solution reach 0, 0.5, 1, and 10 mM, respectively. The samples were then placed on a shaker at 37 °C and 100 rpm. At each designated time point, 2 mL of the sample was withdrawn and centrifuged to gain the supernatant for CUR content analysis. Postcollection, 2 mL of fresh PBS solution was added after each withdrawal to maintain consistent volume throughout the experiment.

The concentration of CUR in the supernatant was measured by an ultraviolet spectrophotometer, recording the absorbance of the sample at 425 nm and calculating the release rate using eq 3.

$$\text{Release rate}\ (\%) = \text{The concentration of CUR in the supernatant}/\text{the concentration of CUR in the original sample} \times 100 \quad (3)$$

Stability Analysis. To assess the pH stability of CUR@CMC-Se, a 15 mL solution (2 mg/mL) was mixed with 15 mL of PBS buffer at varying pH levels (1.2, 6.8, and 7.4) and agitated for 6 h on a shaker (100 rpm, 37 °C). At hourly intervals, 1 mL aliquots were taken out, and 1 mL of fresh PBS was added into the system. The samples were then centrifuged (3000 rpm, 5 min, 4 °C), and the resulting supernatant was collected for further examination.

To simulate gastrointestinal (GIT) conditions, a sequential digestion model was employed, replicating gastric and intestinal phases. Commercially available simulated gastric fluid (SGF) and simulated intestinal fluid (SIF) (Dongguan ChangFeng Technology Co., China) were used, supplemented with digestive enzymes (salivary amylase, pepsin, mucus, and pancreatin) and essential salts ($NaHCO_3$, $MgCl_2$, KCl, K_2PO_4, $(NH_4)_2CO_3$, NaCl, and bile salts).

First, samples were blended with SGF in equal volumes and incubated for 120 min (37 °C and 100 rpm). Following this, the mixtures were combined with SIF in a 1:1 ratio and subjected to an additional 180 min of incubation under the same conditions. After centrifugation (3000 rpm, 5 min, 4 °C), the supernatant was collected for analysis.

The retention rate (%) was calculated as follows

https://doi.org/10.1021/acsnano.4c14373
ACS Nano XXXX, XXX, XXX−XXX

$$\text{Retention rate}\ (\%) = C_{digest}/C_{initial} \times 100 \quad (5)$$

where C_{digest} and $C_{initial}$ represent the concentrations of curcumin in the raw digest and primary raw samples, respectively.

Thermal stability was evaluated by heating a 1 mg/mL solution of CUR@CMC-Se in a 5 mL centrifuge tube at various temperatures (25 °C, 37 °C, 60 °C, 80 °C, and 100 °C) for 6 h. Every 1 h, 2 mL of the sample was diluted with ethanol, and the CUR content was measured at 425 nm by using a UV−visible spectrophotometer.

ROS Detection and Quantification. HT29 cells were seeded in 6-well plates at a density of 2×10^5 cells. Oxidative stressed cells were prepared by adding 400 μM H_2O_2 to the culture medium for 4 h. Thereafter, CUR@CMC-Se was added to the medium for an additional 2 h. After incubation, the medium was removed, and the cells were harvested by centrifugation (1000 rpm for 3 min). The cell pellets were transferred to centrifuge tubes and washed twice with PBS and three times with a serum-free medium. Cells were then stained with DHE for 30 min in an incubator, followed by another centrifugation, and washed three times with serum-free medium. Finally, the cells were resuspended in 1 mL of PBS, and intracellular ROS levels were quantified using a flow cytometer.

Cellular Uptake of CMC-Se-Cy5.5. NHS-activated Cy5.5-NH_2 (1 mg/mL) was gradually mixed with a CMC-Se solution (10 mg/mL). The reaction mass ratio between CMC-Se and Cy5.5-NH_2 was strictly controlled at 100:1. The reaction proceeded with constant stirring for 24 h in the dark. To remove unreacted Cy5.5-NH_2, the resulting CMC-Se-Cy5.5 mixtures were dialyzed against deionized water for 72 h in the dark until no fluorescence was observed in the dialysate. The purified conjugate was then lyophilized and used to prepare Cy5.5-labeled CUR@CMC-Se.

For the cellular uptake study, HT29 cells were plated in 6-well plates at 2×10^5 cells per well and treated with 400 μM H_2O_2 for 4 h to induce oxidative stress. The cells were then incubated with 50 μg/mL CUR@CMC-Se-Cy5.5 for 6 h at 37 °C. After being washed twice with PBS, the cells were treated with 0.025% trypsin−EDTA, collected in microcentrifuge tubes, and resuspended in PBS. Cellular uptake was quantified via flow cytometry.

Data Independent Acquisition (DIA) MS-Based Quantitative Proteomics. *Preparation of Protein Samples.* HT29 cells were cultured overnight and then treated with 400 μM H_2O_2 for 4 h to induce oxidative stress. After harvesting, membrane proteins were extracted using a buffer containing protease and phosphatase inhibitors. Protein concentration was measured via a BCA assay. Cell lysis was performed with a denaturing solution (7 M urea, 2% SDS, 0.1% PMSF, 65 mM DTT). For processing, 50 μg of protein was reduced with TCEP (55 °C, 1 h), alkylated with IAA (25 °C, 40 min), and then acetone-precipitated. Trypsin digestion was carried out overnight.

Establish a Spectral Database. Peptides were fractionated by HPLC using a pH 10.0 ammonium formate/ACN gradient. Six fractions were collected, dried, and stored. For LC−MS/MS analysis, peptides were separated on a C18 column (120 min gradient, 0.1% formic acid/ACN) and analyzed using an Orbitrap Lumos MS. Full-scan MS (120,000 resolution) and HCD-MS/MS (15,000 resolution) were performed. Data were processed with Spectronaut X, searching against Uniprot or custom databases. Fixed (carbamidomethylation) and variable (methionine oxidation) modifications were included with a 1% FDR threshold.

DIA Data Acquisition. A 30 μL portion of 0.1% formic acid aqueous solution was added to each sample. Then, 9 μL of the mixed solution was taken out, and 1 μL of the 10 × iRT peptide was added to the solution. After mixing, it was subjected to nano-LC and analyzed by online electrospray tandem mass spectrometry using an Orbitrap Lumos mass spectrometer with an EASY-nLC 1200 system. 3 μL of the sample was loaded onto an Acclaim PepMap C18 column (75 μm × 25 cm) and separated over 120 min from 5% to 35% of 0.1% formic acid ACN solution at 200 nL/min flow rate and 2 kV electrospray voltage. Mass spectrometry parameters: (1) MS: 350−1500 m/z, 120,000 resolution, 4×10^6 aGC target, 50 ms max injection time; (2) HCD-MS/MS: 30,000 resolution, 1×10^6 aGC target, 32 collision energy, 5% energy increment; and (3) variable window acquisition with 60 windows and 1 m/z overlap.

Bioinformatics Analyses. Proteins should meet two key criteria: detection with a minimum of two distinct peptides and the presence in at least two biological replicates from any experimental group. For differential expression analysis, we applied stringent thresholds by comparing each group against controls and proteins classified as differentially expressed proteins (DEPs) if they exhibited both statistical significance ($p \leq 0.05$) and a meaningful fold change ($\geq$1.2) based on hypergeometric testing. The differentially expressed proteins were enriched on KEGG to find pathways related to Transport and catabolism. The differential proteins on the Transport and catabolism pathways were represented by heat maps.

Validation of the Proteomic Data by qRT-PCR and Western Blot. HT29 cells were seeded in 6-well plates at a density of 200,000 cells per well and treated with 400 μM H_2O_2 for 4 h. Thereafter, total RNA was isolated from the cells using a Trizol reagent. RNA purity was verified by spectrophotometric analysis at 260 and 280 nm. For cDNA synthesis, 1 μg of total RNA was reverse transcribed using Hifair AdvanceFast One-step RT-gDNA Digestion SuperMix for qPCR. The resulting cDNA was then amplified with the SYBR qPCR Mix on a real-time PCR system. Gene expression levels were quantified using the comparative Ct ($2^{-\Delta\Delta Ct}$) method, with β-actin serving as the housekeeping gene for normalization. The primers used in the analysis are listed as follows:

FOLR1: Forward CAAGGTTAAACGACAAGGACAGAC.

Reverse TGAGCCTCCCCTACTACAGC.

To assess the impact of H_2O_2 on key protein levels, we performed Western blot analysis. HT29 cells were plated in a 6-well plate and cultured overnight. The cells were then treated with 400 μM H_2O_2 for 4 h. After treatment, membrane proteins were isolated using a lysis buffer supplemented with protease and phosphatase inhibitors. The protein samples were separated using 10% SDS-PAGE gels via electrophoresis and then blotted onto PVDF membranes. To minimize nonspecific binding, the membranes were treated with 5% BSA for 1 h before incubating with primary antibodies overnight at 4 °C. Afterward, HRP-conjugated secondary antibodies were introduced and reacted for 30 min at 25 °C. Finally, the protein bands were detected using an ECL system and captured using a Canon 9000F Mark II imaging setup. For normalization, Na, K-ATPase served as the loading control. Band intensity was quantified using AlphaEaseFC software to ensure an accurate comparative analysis.

Folic Acid Inhibits Uptake. HT29 cells were treated with 400 μM H_2O_2 for 4 h. Post-treatment, folic acid solutions were incubated with cells for 3 h. Subsequently, the cells were cocultured with CUR@CMC-Se-Cy5.5 (50 μg/mL) at 37 °C for 6 h. Following two rounds of washing with PBS buffer, the nucleus was stained with Hoechst 33,342 and then observed via confocal laser scanning microscopy (CLSM). Moreover, cellular uptake was quantified by flow cytometry.

Animals. Male BALB/C mice, aged between 6 and 8 weeks, were purchased from Beijing Vital River Laboratory Animal Technology Company (Beijing, China) and housed in the SPF animal facility at Shantou University School of Medicine. The study protocol was approved by the animal experiment ethics review board (approval number: SUMC2023-482). Prior to the experiment, all mice underwent a 1 week acclimatization period under standardized conditions: a 12 h light/dark cycle at 25 °C room temperature with ad libitum access to food and water.

Prophylactic Effect of CUR@CMC-Se against DSS-Induced Colitis. The grouping and administration protocols were identical with those of the acute DSS ulcerative colitis model with slight modifications. Briefly, mice received 3% DSS in drinking water for 10 days, along with corresponding drugs for preventive treatment. The control group received distilled water for 10 days without any treatment. Body weight and DAI were monitored to assess inflammation. After the final treatment, mice were fasted for 12 h with access to water and then sacrificed to collect serum, spleen, and colon tissues, which were stored at −80 °C for downstream analysis.

https://doi.org/10.1021/acsnano.4c14373
ACS Nano XXXX, XXX, XXX−XXX

Colonic tissues were horizontally cut 1−2 cm above the anus, cleaned with PBS, fixed in 4% paraformaldehyde, embedded in paraffin, and sectioned into 5 μm slices for pathological sectioning.

Therapeutic Effect of CUR@CMC-Se on DSS-Induced Colitis. Mice were divided into 6 groups (n = 6): Control, DSS, 5-ASA, CUR, CMC-Se, and CUR@CMC-Se. All of the groups received 3% DSS (M_W:36,000 ∼50,000, YEASEN, Shanghai, China) ad libitum in the drinking water for 7 days, while the control group received water, and the DSS solution was refreshed every 2 days. On the seventh day, the drinking of the DSS group was switched to water for an additional 5 days. The 5-ASA group received 5-ASA (200 mg/kg/day), the CUR group received CUR (25 mg/kg/day), the CMC-Se group received CMC-Se (250 mg/kg/day), and the CUR@CMC-Se group received a dose equivalent to 25 mg/kg/day of CUR in the CUR@CMC-Se, administered over 5 days. Body weight and the Disease Activity Index (DAI) were monitored daily throughout the experiment to assess disease progression. After the final treatment, mice were fasted for 12 h with access to water and then sacrificed to collect serum, spleen, and colon tissue, which were stored at −80 °C for downstream analysis. Colonic tissues were horizontally cut 1−2 cm above the anus, cleaned with PBS, fixed in 4% paraformaldehyde and embedded in paraffin, and sectioned into 5 μm slices for pathological sectioning.

Disease Activity Index (DAI) Evaluation. The DAI calculation encompasses the combined scores from weight loss, diarrhea, and the presence of blood in the stool. The scoring guidelines are as follows: for weight loss, no change scores a 0, while losses greater than 1−5%, 5−10%, 10−15%, and over 15% earn points of 1, 2, 3, and 4, respectively. When it comes to stool consistency, normal stools get a 0, while mucous, thin, and watery stools are rated 1, 2, and 3 points, respectively. The stool occult blood test results are scored with 0 for negative, 1 for hint, 2 for moderate, 3 for severe, and 4 for a gross amount of blood.

Biodistribution Study. Mice were divided into control and DSS groups (n = 12). Colitis mice were treated as acute DSS ulcerative colitis models. After the last admission, mice underwent a 24 h fast before being administered 200 μL of CMC-Se-Cy5.5 (1 mg/mL) via oral gavage. The mice were euthanized and dissected at 2, 6, 12, and 24 h. Colon tissue and organs (heart, liver, spleen, lungs, and kidneys) were harvested, and fluorescence signals were visualized using an IVIS imaging system (Caliper Life Sciences, USA).

***In Vivo* ROS Measurement.** To evaluate the efficacy of CUR@CMC-Se in scavenging ROS in inflamed colon tissue, colon specimens obtained from dissection were washed with PBS (pH 7.4) to remove debris and mucus. Subsequently, 100 mg of colon tissue was placed into a grinding tube and mixed with PBS at a 5-fold weight ratio. The tissue was homogenized by using a homogenizer (50 Hz, 60 s), followed by centrifugation at 2000 rpm for 20 min to collect the supernatant. Detection was then performed as per the manufacturer's instructions using a mouse reactive oxygen species enzyme-linked immunosorbent assay kit. OD values for each sample were measured at 450 nm using an ultraviolet spectrophotometer.

Histological Analysis. Paraffin-embedded tissue sections were cut to a standardized thickness of 4 μm and subjected to a graded rehydration series with descending concentrations of ethanol (100%, 100%, 95%, 90%, 80%, and 70%). After rehydration, the sections were stained using hematoxylin (G1004, Servicebio, China) to highlight nuclear structures and eosin (G1001, Servicebio, China) for cytoplasmic and extracellular matrix contrast. A morphological assessment was conducted under a microscope. Each section was systematically scored based on predefined histological criteria outlined in Table S2. The scoring system incorporated multiple parameters, including the severity of inflammatory infiltrates (graded from none to severe), the depth of mucosal injury (ranging from superficial epithelial damage to transmural involvement), and the degree of crypt distortion or loss (assessed as intact, mildly affected, or extensively damaged).

Immunohistochemistry Analysis. Paraffin-embedded tissue sections (4 μm) were deparaffinized, dehydrated, and subjected to antigen retrieval in citrate buffer (pH 6.0). Endogenous peroxidase activity was blocked with 3%H_2O_2, followed by incubation in 3% bovine serum albumin (BSA; GC305010, Servicebio, China) for 30 min. Sections were then incubated overnight at 4 °C with primary antibodies: MPO (GB11224, Servicebio, China, rabbit, 1:200) or ZO-1 (GB111402, Servicebio, China, rabbit, 1:200). After being washed with PBS (pH 7.4), sections were incubated with the HRP-labeled secondary antibody (GB23303, Servicebio, 1:200) for 50 min, followed by DAB staining (G1212, Servicebio, China), hematoxylin counterstaining, dehydration, and mounting. Images were captured using a microscope (E100, Nikon, Japan). The mean integrated optical density (IOD) of each sample was analyzed by using Image-Pro Plus 6.0 (Media Cybernetics, USA) software.

Immunofluorescence Analysis. Paraffin-embedded tissue sections (4 μm) underwent dewaxing and rehydration using environmentally friendly solutions (I/II/III, G1128, Servicebio, Wuhan, China), followed by anhydrous ethanol and water processes. Antigen retrieval was performed using Citrate Antigen Retrieval Solution (0.1 M, pH 6.0) with heating. Sections were blocked with 3% BSA for 30 min and then incubated overnight at 4 °C with primary antibodies: ZO-1 (GB111402, Servicebio, China, rabbit, 1:2500), MPO (GB11224, Servicebio, China, rabbit, 1:2500), Occludin (GB111401, Servicebio, China, rabbit, 1:2500), and MUC2 (GB11344, Servicebio, China, rabbit, 1:2500). After being washed with PBS (pH 7.4), sections were incubated with HRP (Polyclonal Goat Anti-Rabbit IgG) antibodies for 50 min at room temperature (RT). TSA (G1223, Servicebio, China) was used to label the corresponding secondary antibodies. Finally, sections were counterstained with DAPI (G1012, Servicebio, China) for nuclei visualization. Images were acquired using a 3DHISTECH Pannoramic MIDI scanner (Austria), and Image-Pro Plus 6.0 software was used to calculate the mean integrated optical density (IOD) for each sample.

RNA Extraction and qRT-PCR. Total RNA was isolated from colon tissue samples using the Total RNA Extraction Kit (UE-MN-MS-RNA-50, Uelandy, China) in accordance with the manufacturer's instructions. The extracted RNA was then converted to cDNA using HiScript II RT SuperMix for qPCR (+gDNA wiper) (Vazyme, China). qRT-PCR was performed with a THUNDERBIRD SYBR qPCR Mix (TOYOBO, Japan) on a qPT−PCR system (Analytik, Germany). The thermal cycling conditions included an initial denaturation step at 95 °C for 1 min, followed by 40 cycles of 95 °C for 15 s and 60 °C for 30 s. Gene expression was quantified via the $2^{-\Delta\Delta CT}$ method, with β-actin as the housekeeping gene for data normalization. Primer sequences can be found in Table S3.

Enzyme-Linked Immunosorbent Assay (ELISA). The colon tissue samples (100 mg/mL, in PBS) were centrifuged at 10,000 g for 20 min, 4 °C. The supernatants were separated, and the concentrations of occludin-1 and MPO were assessed by ELISA kits (Meimian, China). Additionally, the levels of IL-1, IL-10, and IL-6 in the serum were determined using the corresponding ELISA kits.

16 S Sequencing Analysis. DNA from colon feces was extracted using the E.Z.N.A. Soil DNA Kit (Omega Biotek, Norcross, USA), and its quality was checked by NanoDrop2000 and a 1.0% agarose gel electrophoresis for the next step. The V3−V4 region of the bacterial 16 S rRNA gene was amplified with 338F and 806R primer pairs by a T100 PCR thermocycler. Cycling conditions: initial 95 °C for 3 min, then 27 cycles of 95 °C 30 s, 55 °C 30 s, and 72 °C 45 s, single 72 °C for 10 min, and end at 4 °C. The PCR product was extracted from 2% agarose gel, purified with the kit, and quantified by Qubit 4.0. Purified amplicons were pooled and paired-end sequenced on the Illumina platform by Majorbio. Gut microbiota bioinformatic analysis was performed using the Majorbio Cloud platform.

Determination of Contents of SCFAs. Short-chain fatty acids (SCFAs), including acetic acid, propionic acid, butyric acid, isobutyric acid, and isovaleric acid in fecal samples, were quantified by using gas chromatography. Briefly, standard solutions of each SCFA were prepared at 400 mg/mL based on their densities, and calibration curves were constructed accordingly. 2-Ethylbutyric acid was utilized as an internal standard prepared at a concentration of 10 mg/mL for detection purposes. Fecal samples were weighed and homogenized in distilled water containing 1 M hydrochloric acid to achieve a uniform concentration of 1 mg/mL, with the pH adjusted to approximately

https://doi.org/10.1021/acsnano.4c14373
ACS Nano XXXX, XXX, XXX−XXX

2.5. The homogenates were then subjected to grinding at 50 Hz for 5 min in a cryogenic mill, followed by ultrasonication in an ice bath for 20 min. The samples were subsequently allowed to store at 4 °C for 20 min and centrifuged at 13,000*g* at 4 °C for 10 min, and the supernatants were filtered through a 0.22 μm membrane. 500 μL of the filtered supernatant was transferred to sample vials, to which 20 μL of internal standard application solution (200 μg/mL) was added, followed by thorough mixing with 480 μL of ultrapure water for injection into the GC system. The process is set as follows: (a) injector and detector temperatures set at 250 and 260 °C, respectively; (b) nitrogen was used as the carrier gas with a constant flow rate of 10.3 mL/min; (c) initial column temperature was set at 140 °C and held for 5 min, followed by a gradient increase of 15 °C/min to 180 °C; (d) hydrogen and air flows to the detector were maintained at 40 and 450 mL/min, respectively; and (e) 1 μL injection volume.

During metabolite analysis, the column temperature was adjusted as follows: initial temperature of 140 °C held for 5 min, followed by a gradient increase of 15 °C/min up to 260 °C, maintained for 8 min. Standard solutions and processed samples were injected according to these GC analysis conditions, with all measurements performed in triplicate. After completion of the analyses, SCFA concentrations in samples were calculated based on retention times and peak areas using calibration curves. The standard curve was constructed with concentrations of standard solutions as the *x*-axis (x) and the ratio of peak area of the standard to the internal standard as the *y*-axis (y).

Biosafety Evaluation. Before treatment, the biosafety of CUR@CMC-Se was assessed. Mice were divided into control and CUR@CMC-Se groups (n = 6, evenly split by gender), receiving 500 μL of water and CUR@CMC-Se (25 mg/kg/day), respectively, for 10 days. Body weights were monitored throughout this period. On the 11th day, mice were anesthetized and dissected. Blood was collected via orbital sinus puncture for serum biochemical analysis and complete blood count. Organs including the heart, liver, spleen, lung, and kidney were harvested, washed with PBS, fixed in paraformaldehyde, dehydrated through an alcohol gradient, and embedded in paraffin. Histopathological sections were prepared, stained with H&E, and microscopically examined to assess histological differences between the two groups.

Serum biochemical analysis, complete blood count, and H&E staining of pathological sections were conducted by Wuhan Servicebio Technology Co. Ltd.

Statistics Analysis. The data were analyzed using GraphPad Prism 8.0 from GraphPad Software, Origin 2021 by OriginLab, FlowJo V10 from BD Biosciences, or ImageJ 1.8.0 from the National Institutes of Health. *P* values were calculated using unpaired, two-tailed *t* tests for the comparison of two groups or one-way ANOVA followed by Tukey's post hoc analysis for comparisons involving more than two groups. We considered correlations significant only if the *p*-values were less than 0.05. In each study, samples were randomly distributed across various experimental categories. Measurements were taken from diverse samples rather than from retesting of the same ones. Each data set was the result of at least three independent experiments. The graphic was skillfully crafted through BioRender.com.

ASSOCIATED CONTENT

Supporting Information

The Supporting Information is available free of charge at https://pubs.acs.org/doi/10.1021/acsnano.4c14373.

Synthesis procedure of Se-NHBoc, Se−NH_2, and CMC-Se, chemical structure and ^{1}H spectrum of Se-NHBoc, Se−NH_2, CMC, Se−NH_2, and CMC-Se, characterization of CMC-Se by FTIR, zeta potential, size distribution, XPS, TEM, and ICP-OES, characterization of CUR, CMC-Se, and CUR@CMC-Se by FTIR and DSC, pH stability of CUR@CMC-Se, size distribution of CUR@CMC-Se before and after simulated gastrointestinal digestion, thermal stability of CUR@CMC-Se, biosafety evaluation of CUR@CMC-Se, colon images of mice harvested on day 11 after different treatments from three biologically independent animals in each group, representative images of H&E staining of colon tissue harvested on day 11 after different treatments from three biologically independent animals in each group, immunohistochemical staining analysis of ZO-1, the levels of TNF-α, TGF-β, and IL-6 in the colon tissues measured by RT-qPCR and ELISA on day 13, concentration of SCFAs, disease activity index (DAI) score, histological score in the colon tissues of UC mice, and primers for RT-qPCR (PDF)

AUTHOR INFORMATION

Corresponding Authors

Bo-Bo Zhang − *Department of Biology, College of Science, Shantou University, Shantou 515063 Guangdong, China; Guangdong Provincial Key Laboratory of Marine Biotechnology, Institute of Marine Sciences and Shantou Key Laboratory of Marine Microbial Resources and Interactions with Environment, Shantou University, Shantou 515063, China*; Email: bbzhang@stu.edu.cn

Qiongqiong Yang − *Department of Biology, College of Science, Shantou University, Shantou 515063 Guangdong, China; Guangdong Provincial Key Laboratory of Marine Biotechnology, Institute of Marine Sciences and Shantou Key Laboratory of Marine Microbial Resources and Interactions with Environment, Shantou University, Shantou 515063, China*; orcid.org/0009-0009-9936-2610; Email: qiongqiongyang@stu.edu.cn

Authors

Wo-Qi Cai − *Department of Biology, College of Science, Shantou University, Shantou 515063 Guangdong, China; Guangdong Provincial Key Laboratory of Marine Biotechnology, Institute of Marine Sciences and Shantou Key Laboratory of Marine Microbial Resources and Interactions with Environment, Shantou University, Shantou 515063, China*

Wanqi Liang − *Department of Biology, College of Science, Shantou University, Shantou 515063 Guangdong, China; Guangdong Provincial Key Laboratory of Marine Biotechnology, Institute of Marine Sciences and Shantou Key Laboratory of Marine Microbial Resources and Interactions with Environment, Shantou University, Shantou 515063, China*

Dong Li − *Chemistry and Chemical Engineering Guangdong Laboratory, Shantou 515031, China*

Wenli Dai − *Department of Biology, College of Science, Shantou University, Shantou 515063 Guangdong, China; Guangdong Provincial Key Laboratory of Marine Biotechnology, Institute of Marine Sciences and Shantou Key Laboratory of Marine Microbial Resources and Interactions with Environment, Shantou University, Shantou 515063, China*

Zhishu Li − *Department of Biology, College of Science, Shantou University, Shantou 515063 Guangdong, China; Guangdong Provincial Key Laboratory of Marine Biotechnology, Institute of Marine Sciences and Shantou Key Laboratory of Marine Microbial Resources and Interactions with Environment, Shantou University, Shantou 515063, China*

https://doi.org/10.1021/acsnano.4c14373
ACS Nano XXXX, XXX, XXX−XXX

Xinlin Wei − *School of Agriculture and Biology, Shanghai Jiao Tong University, Shanghai 200240, China;* orcid.org/0000-0002-7389-5330

Lizeng Cheng − *School of Agriculture and Biology, Shanghai Jiao Tong University, Shanghai 200240, China*

Complete contact information is available at: https://pubs.acs.org/10.1021/acsnano.4c14373

Author Contributions

#W-Q.C., W.L., and D.L. contributed equally to this work. The manuscript was written through contributions of all authors. All authors have given approval to the final version of the manuscript. W. Q. C., W. L., and D. L. contributed to the design and completion of the study. W. D., Z. L., X. L., and L. C. made contributions to cell experiments, animal experiments, and manuscript revision. B. B. Z. and Q. Y. supported this study. All authors discussed and contributed to the interpretation of the results.

Funding

This work was supported by the National Natural Science Foundation of China (32302280), National Natural Science Foundation of China (32472313), National Natural Science Foundation of China (32072184), Special Funding Program for Guangdong Science and Technology Innovation Strategic Project (STKJ202209022), and Research Start-up Foundation of Shantou University (NTF22003).

Notes

The authors declare no competing financial interest.

REFERENCES

(1) Guo, X.; Xu, Y.; Geng, R.; Qiu, J.; He, X. Curcumin Alleviates Dextran Sulfate Sodium-Induced Colitis in Mice Through Regulating Gut Microbiota. *Mol. Nutr. Food Res.* **2022**, *66*, 2100943.

(2) Tan, C.; Fan, H.; Ding, J.; Han, C.; Guan, Y.; Zhu, F.; Wu, H.; Liu, Y.; Zhang, W.; Hou, X.; Tan, S.; Tang, Q. ROS-Responsive Nanoparticles for Oral Delivery of Luteolin and Targeted Therapy of Ulcerative Colitis by Regulating Pathological Microenvironment. *Mater. Today Bio.* **2022**, *14*, 100246.

(3) Ng, S. C.; Shi, H. Y.; Hamidi, N.; Underwood, F. E.; Tang, W.; Benchimol, E. I.; Panaccione, R.; Ghosh, S.; Wu, J. C. Y.; Chan, F. K. L.; Sung, J. J.; Kaplan, G. G. Worldwide Incidence and Prevalence of Inflammatory Bowel Disease in the 21st Century: a Systematic Review of Population-Based Studies. *Lancet.* **2017**, *390*, 2769−2778.

(4) Chu, X. Q.; Wang, J.; Chen, G. X.; Zhang, G. Q.; Zhang, D. Y.; Cai, Y. Y. Overexpression of Microrna-495 Improves the Intestinal Mucosal Barrier Function by Targeting STAT3 *via* Inhibition of the JAK/STAT3 Signaling Pathway in a Mouse Model of Ulcerative Colitis. *Pathol Res. Pract.* **2018**, *214*, 151−162.

(5) Liang, D.; Shen, X.; Han, L.; Ren, H.; Zang, T.; Tan, L.; Lu, Z.; Liao, X.; Vetha, B. S. S.; Liu, Y.; Zhang, C.; Sun, J. Dual-ROS Sensitive Moieties Conjugate Inhibits Curcumin Oxidative Degradation for Colitis Precise Therapy. *Adv. Healthc Mater.* **2024**, *13*, 2303016.

(6) Fang, X.; Feng, J.; Zhu, X.; Feng, D.; Zheng, L. Plant-Derived Vesicle-Like Nanoparticles: a New Tool for Inflammatory Bowel Disease and Colitis-Associated Cancer Treatment. *Mol. Ther.* **2024**, *32*, 890−909.

(7) Park, J.; Cheon, J. H. Updates on Conventional Therapies for Inflammatory Bowel Diseases: 5-Aminosalicylates, Corticosteroids, Immunomodulators, and Anti-TNF-α. *Korean J. Intern Med.* **2022**, *37*, 895−905.

(8) Liu, Y.; Cheng, Y.; Zhang, H.; Zhou, M.; Yu, Y.; Lin, S.; Jiang, B.; Zhao, X.; Miao, L.; Wei, C.; Liu, Q.; Lin, Y.; Du, Y.; Butch, C. J.; Wei, H. Integrated Cascade Nanozyme Catalyzes *in Vivo* ROS Scavenging for Anti-Inflammatory Therapy. *Sci. Adv.* **2020**, *6*, No. eabb2695.

(9) Hao, Y.; Song, K.; Tan, X.; Ren, L.; Guo, X.; Zhou, C.; Li, H.; Wen, J.; Meng, Y.; Lin, M.; Zhang, Y.; Huang, H.; Wang, L.; Zheng, W. Reactive Oxygen Species-Responsive Polypeptide Drug Delivery System Targeted Activated Hepatic Stellate Cells to Ameliorate Liver Fibrosis. *ACS Nano.* **2022**, *16*, 20739−20757.

(10) Fan, W.; Zhang, S.; Wu, Y.; Lu, T.; Liu, J.; Cao, X.; Liu, S.; Yan, L.; Shi, X.; Liu, G.; Huang, G.; Song, S. Genistein-Derived ROS-Responsive Nanoparticles Relieve Colitis by Regulating Mucosal Homeostasis. *ACS Appl. Mater. Inter.* **2021**, *13*, 40249−40266.

(11) Zhou, J.; Fang, C.; Rong, C.; Luo, T.; Liu, J.; Zhang, K. Reactive Oxygen Species-Sensitive Materials: a Promising Strategy for Regulating Inflammation and Favoring Tissue Regeneration. *Smart Mater. Med.* **2023**, *4*, 427−446.

(12) Uthaman, S.; Parvinroo, S.; Mathew, A. P.; Jia, X. L.; Hernandez, B.; Proctor, A.; Sajeevan, K. A.; Nenninger, A.; Long, M. J.; Park, I. K.; Chowdhury, R.; Phillips, G. J.; Wannemuehler, M. J.; Bardhan, R. Inhibiting the Cgas-STING Pathway in Ulcerative Colitis with Programmable Micelles. *ACS Nano.* **2024**, *18*, 12117−12133.

(13) Xu, J.; Chu, T.; Yu, T.; Li, N.; Wang, C.; Li, C.; Zhang, Y.; Meng, H.; Nie, G. Design of Diselenide-Bridged Hyaluronic Acid Nano-Antioxidant for Efficient ROS Scavenging to Relieve Colitis. *ACS Nano.* **2022**, *16*, 13037−13048.

(14) Pu, M.; Cao, H.; Zhang, H.; Wang, T.; Li, Y.; Xiao, S.; Gu, Z. ROS-Responsive Hydrogels: from Design and Additive Manufacturing to Biomedical Applications. *Mater. Horiz.* **2024**, *11*, 3721−3746.

(15) Yousefiasl, S.; Sharifi, E. Reactive Oxygen Species-Responsive Compounds: Properties, Design, and Applications. *Stimuli-Responsive Mater. Biomed. Appl.* **2023**, *1436*, 181−201.

(16) Birhan, Y. S.; Tsai, H. C. Recent Developments in Selenium-Containing Polymeric Micelles: Prospective Stimuli, Drug-Release Behaviors, and Intrinsic Anticancer Activity. *J. Mater. Chem. B.* **2021**, *9*, 6770−6801.

(17) Li, T.; Pan, S.; Gao, S.; Xiang, W.; Sun, C.; Cao, W.; Xu, H. Diselenide-Pemetrexed Assemblies for Combined Cancer Immuno, Radio, and Chemotherapies. *Angew. Chem., Int. Ed.* **2020**, *59*, 2700−2704.

(18) Gao, S.; Li, T.; Guo, Y.; Sun, C.; Xianyu, B.; Xu, H. Selenium-Containing Nanoparticles Combine the NK Cells Mediated Immunotherapy with Radiotherapy and Chemotherapy. *Adv. Mater.* **2020**, *32*, 1907568.

(19) Nogueira, C. W.; Rocha, J. B. T. Diphenyl Diselenide a Janus-Faced Molecule. *J. Braz. Chem. Soc.* **2010**, *21*, 2055−2071.

(20) Nogueira, C. W.; Zeni, G.; Rocha, J. B. T. Organoselenium and Organotellurium Compounds: Toxicology and Pharmacology. *Chem. Rev.* **2004**, *104*, 6255−6286.

(21) Zennifer, A.; Senthilvelan, P.; Sethuraman, S.; Sundaramurthi, D. Key Advances of Carboxymethyl Cellulose in Tissue Engineering & 3D Bioprinting Applications. *Carbohydr. Polym.* **2021**, *256*, 117561.

(22) Kumar, R.; Islam, T.; Nurunnabi, M. Mucoadhesive Carriers for Oral Drug Delivery. *J. Controlled Release.* **2022**, *351*, 504−559.

(23) Kudelka, M. R.; Stowell, S. R.; Cummings, R. D.; Neish, A. S. Intestinal Epithelial Glycosylation in Homeostasis and Gut Microbiota Interactions in IBD. *Nat. Rev. Gastro Hepat.* **2020**, *17*, 597−617.

(24) Zhang, L.; Gui, S.; Xu, Y.; Zeng, J.; Wang, J.; Chen, Q.; Su, L.; Wang, Z.; Deng, R.; Chu, F.; Liu, W.; Jin, X.; Lu, X. Colon Tissue-Accumulating Mesoporous Carbon Nanoparticles Loaded with *Musca Domestica* Cecropin for Ulcerative Colitis Therapy. *Theranostics.* **2021**, *11*, 3417−3438.

(25) Zhang, S.; Kang, L.; Hu, S.; Hu, J.; Fu, Y.; Hu, Y.; Yang, X. Carboxymethyl Chitosan Microspheres Loaded Hyaluronic Acid/Gelatin Hydrogels for Controlled Drug Delivery and the Treatment of Inflammatory Bowel Disease. *Int. J. Biol. Macromol.* **2021**, *167*, 1598−1612.

(26) Yang, Q. Q.; Farha, A. K.; Kim, G.; Gul, K.; Gan, R. Y.; Corke, H. Antimicrobial and Anticancer Applications and Related Mechanisms of Curcumin-Mediated Photodynamic Treatments. *Trends Food Sci. Tech.* **2020**, *97*, 341−354.

(27) Chen, F. Q.; Liu, Q. Demystifying Phytoconstituent-Derived Nanomedicines in Their Immunoregulatory and Therapeutic Roles in Inflammatory Diseases. *Adv. Drug Deliv.* **2022**, *186*, 114317.
(28) Wei, C.; Wang, J. Y.; Xiong, F.; Wu, B. H.; Luo, M. H.; Yu, Z. C.; Liu, T. T.; Li, D. F.; Tang, Q.; Li, Y. X.; Zhang, D. G.; Xu, Z. L.; Jin, H. T.; Wang, L. S.; Yao, J. Curcumin Ameliorates DSS-Induced Colitis in Mice by Regulating the Treg/Th17 Signaling Pathway. *Mol. Med. Rep.* **2020**, *23*, 34.
(29) Peterson, C. T.; Vaughn, A. R.; Sharma, V.; Chopra, D.; Mills, P. J.; Peterson, S. N.; Sivamani, R. K. Effects of Turmeric and Curcumin Dietary Supplementation on Human Gut Microbiota: a Double-Blind, Randomized, Placebo-Controlled Pilot Study. *J. Evid Based Integr Med.* **2018**, *23*, 2515690× 18790725.
(30) Zam, W. Gut Microbiota As a Prospective Therapeutic Target for Curcumin: a Review of Mutual Influence. *J. Nutr Metab.* **2018**, *2018*, 1−11.
(31) Yang, M.; Liu, J.; Liu, C.; Zhang, H.; Li, S.; Zhang, T.; Yu, Z.; Chi, X.; Zhang, Z.; Du, Z. Programmable Food-Derived Peptide Coassembly Strategies for Boosting Targeted Colitis Therapy by Enhancing Oral Bioavailability and Restoring Gut Microenvironment Homeostasis. *ACS Nano.* **2025**, *19*, 600−620.
(32) Cai, W. Q.; Liu, X.; Chen, W.; Huang, Z.; Li, C.; Huang, X.; Harold, C.; Su, B. L.; Zhang, B. B.; Yang, Q. Q. Synergistic Effect of Lecithin and Alginate, CMC, or PVP in Stabilizing Curcumin and Its Potential Mechanism. *Food Chem.* **2023**, *413*, 135634.
(33) Chuang, E. Y.; Lin, K. J.; Huang, T. Y.; Chen, H. L.; Miao, Y. B.; Lin, P. Y.; Chen, C. T.; Juang, J. H.; Sung, H. W. An Intestinal "Transformers"-Like Nanocarrier System for Enhancing the Oral Bioavailability of Poorly Water-Soluble Drugs. *ACS Nano.* **2018**, *12*, 6389−6397.
(34) Pituch-Zdanowska, A.; Dembinski, L.; Banaszkiewicz, A. Old But Fancy: Curcumin in Ulcerative Colitis-Current Overview. *Nutrients.* **2022**, *14* (24), 5249.
(35) Jo, Y. J.; Gulfam, M.; Jo, S. H.; Gal, Y. S.; Oh, C. W.; Park, S. H.; Lim, K. T. Multi-Stimuli Responsive Hydrogels Derived from Hyaluronic Acid for Cancer Therapy Application. *Carbohydr. Polym.* **2022**, *286*, 119303.
(36) Wang, J.; Liu, J.; Lu, D. Q.; Chen, L.; Yang, R.; Liu, D.; Zhang, B. Diselenide-Crosslinked Carboxymethyl Chitosan Nanoparticles for Doxorubicin Delivery: Preparation and *in Vivo* Evaluation. *Carbohydr. Polym.* **2022**, *292*, 119699.
(37) Anugrah, D. S. B.; Ramesh, K.; Kim, M.; Hyun, K.; Lim, K. T. Near-Infrared Light-Responsive Alginate Hydrogels Based on Diselenide-Containing Cross-Linkage for on Demand Degradation and Drug Release. *Carbohydr. Polym.* **2019**, *223*, 115070.
(38) Szegedi, A. ·; Shestakova, P.; Trendafilova, I.; Mihayi, J.; Tsacheva, I.; Mitova, V.; Kyulavska, M.; Koseva, N.; Momekova, D.; Konstantinov, S.; Aleksandrov, H. A.; St Petkov, P.; Koleva, I. Z.; Vayssilov, G. N.; Popova, M. Modified Mesoporous Silica Nanoparticles Coated by Polymer Complex As Novel Curcumin Delivery Carriers. *J. Drug Deliv Sci. Tec* **2019**, *49*, 700−712.
(39) Zeng, Q.; Zeng, W.; Jin, Y.; Sheng, L. Construction and Evaluation of Ovalbumin-Pullulan Nanogels As a Potential Delivery Carrier for Curcumin. *Food Chem.* **2022**, *367*, 130716.
(40) Chen, T.; Meng, W.; Li, Y.; Li, X.; Yu, X.; Qi, J.; Ding, D.; Li, W. Probiotics Armed with *in Situ* Mineralized Nanocatalysts and Targeted Biocoatings for Multipronged Treatment of Inflammatory Bowel Disease. *Nano Lett.* **2024**, *24* (24), 7321−7331.
(41) Chung, C. H.; Jung, W.; Keum, H.; Kim, T. W.; Jon, S. Nanoparticles Derived from the Natural Antioxidant Rosmarinic Acid Ameliorate Acute Inflammatory Bowel Disease. *ACS Nano.* **2020**, *14*, 6887−6896.
(42) Neurath, M. F. Strategies for Targeting Cytokines in Inflammatory Bowel Disease. *Nat. Rev. Immunol.* **2024**, *24*, 559−576.
(43) Wang, C. P. J.; Byun, M. J.; Kim, S. N.; Park, W.; Park, H. H.; Kim, T. H.; Lee, J. S.; Park, C. G. Biomaterials As Therapeutic Drug Carriers for Inflammatory Bowel Disease Treatment. *J. Controlled Release.* **2022**, *345*, 1−19.
(44) Guo, R. B.; Zhang, X. Y.; Yan, D. K.; Yu, Y. J.; Wang, Y. J.; Geng, H. X.; Wu, Y. N.; Liu, Y.; Kong, L.; Li, X. T. Folate-Modified Triptolide Liposomes Target Activated Macrophages for Safe Rheumatoid Arthritis Therapy. *Biomater. Sci.* **2022**, *10*, 499−513.
(45) Liang, W.; Li, D.; Hao, J.; Dai, W.; Zhang, B. B.; Yang, Q. Cellular Uptake Mechanisms of Diselenide-Based ROS-Responsive Nanocarrier in Oxidatively Stressed Colon Cells. *Chem. Comm.* **2025**, *61*, 4339−4342.
(46) Thottacherry, J. J.; Sathe, M.; Prabhakara, C.; Mayor, S. Spoiled for Choice: Diverse Endocytic Pathways Function at the Cell Surface. *Annu. Rev. Cell Dev. Biol.* **2019**, *35*, 55−84.
(47) Ahmed, O.; Farid, A.; Elamir, A. Dual Role of Melatonin As an Anti-Colitis and Anti-Extra Intestinal Alterations Against Acetic Acid-Induced Colitis Model in Rats. *Sci. Rep-UK.* **2022**, *12*, 6344.
(48) Liu, C.; He, Y. X.; Zhang, J. N.; Yang, F.; Wang, S. Y.; Hu, J. L.; Yu, Y. Angelica Oil Restores the Intestinal Barrier Function by Suppressing S100A8/A9 Signalling in Mice with Ulcerative Colitis. *Phytomed.* **2023**, *108*, 154490.
(49) Li, J.; Ding, F.; Qian, X.; Sun, J.; Ge, Z.; Yang, L.; Cheng, Z. Anti-Inflammatory Cytokine IL10 Loaded Crgd Liposomes for the Targeted Treatment of Atherosclerosis. *J. Microencapsul.* **2021**, *38*, 357−364.
(50) Liu, J.; Wang, Y.; Heelan, W. J.; Chen, Y.; Li, Z.; Hu, Q. Mucoadhesive Probiotic Backpacks with ROS Nanoscavengers Enhance the Bacteriotherapy for Inflammatory Bowel Diseases. *Sci. Adv.* **2022**, *8* (45), No. eabp8798.
(51) Li, Y.; Liu, J.; Shi, X.; Li, S.; Zhang, H.; Zhang, L.; Huang, X.; Liu, S.; Wang, W.; Tian, L.; Zhang, T.; Du, Z. Casein-Quaternary Chitosan Complexes Induced the Soft Assembly of Egg White Peptide and Curcumin for Ulcerative Colitis Alleviation. *Int. J. Biol. Macromol.* **2024**, *269*, 132107.
(52) Zhang, D.; Jian, Y. P.; Zhang, Y. N.; Li, Y.; Gu, L. T.; Sun, H. H.; Liu, M. D.; Zhou, H. L.; Wang, Y. S.; Xu, Z. X. Short-Chain Fatty Acids in Diseases. *Cell Commun. Signal.* **2023**, *21*, 212.
(53) Li, H.; Wang, Y.; Shao, S.; Yu, H.; Wang, D.; Li, C.; Yuan, Q.; Liu, W.; Cao, J.; Wang, X.; Guo, H.; Wu, X.; Wang, S. *Rabdosia Serra* Alleviates Dextran Sulfate Sodium Salt-Induced Colitis in Mice Through Anti-Inflammation, Regulating Th17/Treg Balance, Maintaining Intestinal Barrier Integrity, and Modulating Gut Microbiota. *J. Pharm. Anal.* **2022**, *12*, 824−838.
(54) Liu, M. J.; Yang, J. Y.; Yan, Z. H.; Hu, S.; Li, J. Q.; Xu, Z. X.; Jian, Y. P. Recent Findings in *Akkermansia Muciniphila*-Regulated Metabolism and Its Role in Intestinal Diseases. *Clin Nutr.* **2022**, *41*, 2333−2344.
(55) van der Lugt, B.; van Beek, A. A.; Aalvink, S.; Meijer, B.; Sovran, B.; Vermeij, W. P.; Brandt, R. M. C.; de Vos, W. M.; Savelkoul, H. F. J.; Steegenga, W. T.; Belzer, C. *Akkermansia Muciniphila* Ameliorates the Age-Related Decline in Colonic Mucus Thickness and Attenuates Immune Activation in Accelerated Aging Ercc1-/Δ7 Mice. *Immun Ageing.* **2019**, *16*, 6.
(56) Shi, M.; Yue, Y.; Ma, C.; Dong, L.; Chen, F. Pasteurized *Akkermansia Muciniphila* Ameliorate the LPS-Induced Intestinal Barrier Dysfunction *via* Modulating AMPK and NF-KB Through TLR2 in Caco-2 Cells. *Nutrients.* **2022**, *14*, 764.
(57) Xiao, B.; Xu, Z.; Viennois, E.; Zhang, Y.; Zhang, Z.; Zhang, M.; Han, M. K.; Kang, Y.; Merlin, D. Orally Targeted Delivery of Tripeptide KPV *via* Hyaluronic Acid-Functionalized Nanoparticles Efficiently Alleviates Ulcerative Colitis. *Mol. Ther.* **2017**, *25*, 1628−1640.
(58) Guo, X. Y.; Liu, X. J.; Hao, J. Y. Gut Microbiota in Ulcerative Colitis: Insights on Pathogenesis and Treatment. *J. Dig Dis.* **2020**, *21*, 147−159.
(59) Cao, F.; Jin, L.; Gao, Y.; Ding, Y.; Wen, H.; Qian, Z.; Zhang, C.; Hong, L.; Yang, H.; Zhang, J.; Tong, Z.; Wang, W.; Chen, X.; Mao, Z. Artificial-Enzymes-Armed *Bifidobacterium Longum* Probiotics for Alleviating Intestinal Inflammation and Microbiota Dysbiosis. *Nat. Nanotechnol.* **2023**, *18*, 617−627.
(60) Hartwig, O.; Shetab Boushehri, M. A.; Shalaby, K. S.; Loretz, B.; Lamprecht, A.; Lehr, C. M. Drug Delivery to the Inflamed

https://doi.org/10.1021/acsnano.4c14373
ACS Nano XXXX, XXX, XXX−XXX

Intestinal Mucosa-Targeting Technologies and Human Cell Culture Models for Better Therapies of IBD. *Adv. Drug Deliv.* **2021**, *175*, 113828.
(61) Liu, J.; Yuan, S. C.; Bremmer, A.; Hu, Q. Convergence of Nanotechnology and Bacteriotherapy for Biomedical Applications. *Adv. Sci.* **2024**, *11* (16), 2309295.
(62) Peng, H.; Wang, C.; Xu, X.; Yu, C.; Wang, Q. An Intestinal Trojan Horse for Gene Delivery. *Nanoscale.* **2015**, *7* (10), 4354–4360.
(63) Zhang, S.; Ermann, J.; Succi, M. D.; Zhou, A.; Hamilton, M. J.; Cao, B.; Korzenik, J. R.; Glickman, J. N.; Vemula, P. K.; Glimcher, L. H.; Traverso, G.; Langer, R.; Karp, J. M. An Inflammation-Targeting Hydrogel for Local Drug Delivery in Inflammatory Bowel Disease. *Sci. Transl. Med.* **2015**, *7* (300), 300ra128.
(64) Zhang, J.; Zhao, Y.; Hou, T.; Zeng, H.; Kalambhe, D.; Wang, B.; Shen, X.; Huang, Y. Macrophage-Based Nanotherapeutic Strategies in Ulcerative Colitis. *J. Controlled Release.* **2020**, *320*, 363–380.
(65) Li, S.; Zhang, F.; Zhang, Q. Pathological Features-Based Targeted Delivery Strategies in IBD Therapy: a Mini Review. *Biomed Pharmacother.* **2022**, *151*, 113079.
(66) Klinke, A.; Nussbaum, C.; Kubala, L.; Friedrichs, K.; Rudolph, T. K.; Rudolph, V.; Paust, H. J.; Schroeder, C.; Benten, D.; Lau, D.; Szocs, K.; Furtmueller, P.; Heeringa, P.; Sydow, K.; Duchstein, H. J.; Ehmke, H.; Schumacher, U.; Meinertz, T.; Sperandio, M.; Baldus, S. Myeloperoxidase Attracts Neutrophils by Physical Forces. *Blood.* **2011**, *117* (4), 1350–1358.
(67) Sharkey, K. A.; Beck, P. L.; McKay, D. M. Neuroimmunophysiology of the Gut: Advances and Emerging Concepts Focusing on the Epithelium. *Nat. Rev. Gastro Hepat.* **2018**, *15*, 765–784.

https://doi.org/10.1021/acsnano.4c14373
ACS Nano XXXX, XXX, XXX–XXX